

# Separation of long-range and short-range interactions in Rydberg states of diatomic molecules

Jeffrey J. Kay, Stephen L. Coy, Vladimir S. Petrović, Bryan M. Wong, and Robert W. Field<sup>a)</sup>

*Department of Chemistry, Massachusetts Institute of Technology, Cambridge, Massachusetts 02139, USA*

(Received 10 December 2007; accepted 19 March 2008; published online 15 May 2008)

Observation and analysis of the  $f(\ell=3)$ ,  $g(\ell=4)$ , and  $h(\ell=5)$  Rydberg series of CaF in the range  $13 \leq n \leq 17$  is presented. Simultaneous analysis of the  $f$ ,  $g$ , and  $h$  Rydberg series of CaF, combined with significant improvements to the long-range model for nonpenetrating Rydberg states, provides a generally applicable scheme for separating the effects of the long-range (electric multipole and polarization) and short-range (core penetration) interactions between the Rydberg electron and ion core in diatomic molecules. Techniques for rigorous assignment of nonpenetrating states, as well as extensions of the long-range model, are discussed. Explicit formulas for the first- and second-order matrix elements of the first four anisotropic electric multipole interactions (electric dipole, quadrupole, octupole, and hexadecapole) are given. The discrepancies between the observed behavior and that predicted by the long-range model, which are particularly significant for the  $f$  series, are shown to be due to penetration of the Rydberg electron wavefunction within the ion core. We show that these penetration effects can be understood within the framework of ligand field theory and conclude with a discussion of the relative contributions of the long- and short-range interactions to the quantum defects of the core-penetrating “ $s$ ,” “ $p$ ,” and “ $d$ ” series of CaF.

© 2008 American Institute of Physics. [DOI: [10.1063/1.2907858](https://doi.org/10.1063/1.2907858)]

## I. INTRODUCTION

The Rydberg states of atoms and molecules are usually organized into two very distinct categories, according to the nature of the orbit of the excited electron: Rydberg states are termed “core-penetrating” when the wavefunction of the Rydberg electron has significant amplitude inside the inner electron shells, and are termed “core nonpenetrating” when it does not. Although only a small fraction of the probability density of the Rydberg electron wavefunction lies near the nuclei in both cases, the degree to which the electron wavefunction penetrates inside the inner electron shells has a profound impact on the properties of the state in question.

Structurally and conceptually, nonpenetrating states are generally simpler than penetrating states. Since in nonpenetrating states the outer electron does not enter the region of space occupied by the inner electron shells, its wavefunction has no overlap with that of the core electrons. Thus, one only needs to consider the long-range forces between the electron and ion core: The electrostatic interactions through the multipole fields of the core and the polarization of the core by the outer electron. This “long-range model” has been successfully applied to both atoms and molecules numerous times with great success.<sup>1–5</sup>

In penetrating states, on the other hand, the wavefunction of the outer electron does overlap that of the core electrons and consequently experiences not only the long-range interactions described above but also Coulomb and exchange interactions with the inner electrons at short range. Calculations of the properties of core-penetrating Rydberg states are

therefore inherently more complicated. However, this increased complexity is offset by a dramatic increase in richness of dynamical behavior: On account of the overlap with the core orbitals, penetrating Rydberg states participate in important chemical processes such as dissociation and electron rearrangements, and penetrating Rydberg orbitals often display bonding and antibonding behavior. Indeed, almost *all* of the chemical behavior of molecules depends on these types of interactions at short range.

While the short-range part of the problem is in principle quite complicated, quantum defect theory,<sup>6</sup> which has evolved as a useful tool for describing all Rydberg states on an equal footing, sidesteps the multielectron nature of the problem by only considering the net effect of the short-range interactions on the wavefunction outside the inner electron shells, i.e., the wavefunction’s radial phase shifts. By knowing the phase shifts of the electronic wavefunctions of all of the Rydberg series (or alternately, their quantum defects), one has in principle complete knowledge of the system and the ability to calculate any of its spectroscopic or dynamical properties.

Aside from their computational utility, these phase shifts (or quantum defects) also provide a wealth of insight into the interactions the electron experiences inside the core. In our study of CaF, the subject of the current work, we have determined all of the quantum defects of the molecule at its equilibrium geometry and most of their first derivatives with respect to internuclear distance. Another large-scale quantum defect fit is currently underway and will provide more accurate and more complete information on the dependencies of the quantum defects on the internuclear distance *and* on the collision energy of the outer electron. Our ultimate goal is to

<sup>a)</sup>Electronic mail: [rwfield@mit.edu](mailto:rwfield@mit.edu).

understand *why* these quantum defects have the values that they do and why they vary with molecular geometry and collision energy in the way that they do, in the hope that an intuitive understanding of the short-range interactions between the electron and ion will permit a deeper understanding of the chemical behavior of the molecule.

However, if we really wish to understand the interactions that occur at short range, we must first separate them from the interactions that occur at long range. This is the goal of the current investigation. Our approach to separating the long-range and short-range interactions is to apply the long-range model first to strictly nonpenetrating Rydberg states with high orbital angular momentum, which allows us to accurately determine the strength of the most important long-range interactions. We then apply the long-range model to Rydberg series with progressively greater core-penetrating character. By knowing the explicit forms of all possible long-range interactions, as well as maximum values for each associated adjustable parameter, we are able to exploit significant deviations between the observed behavior and that calculated by the long-range model to quantitatively describe core penetration effects. This allows us to explicitly determine the portion of each quantum defect that is due to interactions at short range and to achieve the desired separation of long-range and short-range effects. Finally, having separated the core-penetration effects, we discuss their physical origins.

## II. EXPERIMENT

### A. Double resonance spectra

To access states of high orbital angular momentum in CaF, we have recorded new ionization-detected double resonance spectra covering the range  $n^*=12.5$ ,  $v=1$  (total energy  $\sim 47\,000\text{ cm}^{-1}$  relative to the  $N=0$ ,  $v=0$  level of the  $X\ ^2\Sigma^+$  ground state) to  $n^*=17.5$ ,  $v=1$  (total energy  $\sim 47\,325\text{ cm}^{-1}$  relative to the ground state), using appropriate rovibrational levels of the  $F'\ ^2\Sigma^+$  state as intermediates. This energy range begins roughly at the energy of the first ionization potential of CaF [ $\text{CaF}^+(v^+=0, N^+=0) + e^-$ ] and was specifically chosen because: (i)  $\ell$  uncoupling is strong even at low  $N$  in the  $n^*=12.5\text{--}17.5$  range, which allows access to nominally dark high- $\lambda$  ( $f\varphi$ ,  $g\gamma$ , etc.) Rydberg states, and (ii) above the first ionization potential, Rydberg states are both excited and (auto-) ionized by absorption of a single photon from the  $F'\ ^2\Sigma^+$  intermediate state, which allows us to record spectra with an extremely high signal-to-noise ratio and consequently admits the possibility of observing very weak transitions into Rydberg states with high orbital angular momentum ( $\ell \geq 5$ ).

The  $F'\ ^2\Sigma^+$  state was chosen as the intermediate state in the double resonance experiments because it is the terminus of the “ $d$ ”  $^2\Sigma^+$  Rydberg series of CaF ( $n^*=3.18$ ; nominal Ca<sup>3</sup> $d$  character). This significant  $d$  character leads us to expect strong upward transitions to  $f$  states. Additionally, since  $\text{CaF}^+$  is known to have an enormous center-of-mass dipole moment [approximately 9 D or 3.5 a.u. (Ref. 7)], we expect that moderate  $nf \sim ng$  mixing should occur, and  $g$  states should also be observable, via their admixed  $f$  character.

The experimental apparatus has been described in detail elsewhere.<sup>8</sup> Briefly, a laser ablation/molecular beam source is coupled to a time-of-flight mass spectrometer, housed in separately-pumped “source” and “detection” vacuum chambers. A molecular beam of calcium monofluoride is produced in the source chamber by direct reaction of calcium plasma with fluorine. A 350  $\mu\text{s}$  pulse of 5%  $\text{CHF}_3$  in He formed by a pulsed nozzle (General Valve Series 9, 0.5 mm orifice, 40 psi stagnation pressure, 20 Hz duty cycle) is synchronized with the pulsed production of a calcium plasma formed by laser ablation of a rotating 1/4 in. diameter calcium rod by the third harmonic of a pulsed Nd:YAG (YAG denotes yttrium aluminum garnet) laser (Spectra Physics GCR-130, 5–7 ns pulse, 7 mJ/pulse, 20 Hz repetition rate). The duration of the fluorine pulse and the energy of the ablation laser are both adjusted to optimize the production of CaF and to reduce the amount of unreacted calcium.  $\text{Ca}^+$  ( $m/z=40$ ) and  $\text{CaF}^+$  ( $m/z=59$ ) are the dominant ions observed and no other ions with greater than 5% of the intensity of the  $\text{CaF}^+$  ion signal are observed. The rotational temperature of the molecular beam is  $\sim 30\text{ K}$ . The molecular beam is collimated by a 0.5 mm conical skimmer placed between the source and detection chambers, and again by a 3.0 mm skimmer prior to entering the excitation region of the detection chamber. CaF Rydberg states are populated and ionized in the detection chamber by two collinear laser beams that intersect the molecular beam at a  $90^\circ$  angle. The  $\text{CaF}^+$  ions that result are accelerated down the 75 cm flight tube of the mass spectrometer by a 250 V electric field pulse that arrives 200 ns after the laser excitation pulse. Ions are detected by two microchannel plates (Burle Electrooptics, 10  $\mu\text{m}$  channel diameter, 12  $\mu\text{m}$  channel spacing) arranged in a chevron configuration. The ion signals are amplified by a low-noise voltage amplifier (FemtoAmp, 30 dB gain, 30 MHz lowpass filter) and averaged over 40 shots by a LeCroy 1 GHz digital oscilloscope.

CaF Rydberg states lying between  $n^*=12.5$ ,  $v=1$  ( $\sim 47\,000\text{ cm}^{-1}$ ) and  $n^*=17.5$ ,  $v=1$  ( $47\,325\text{ cm}^{-1}$ ), are accessed by two-step excitation through the  $F'\ ^2\Sigma^+$  intermediate state. Pump and probe laser pulses are produced by two pulsed dye lasers (Lambda Physik Scanmate 2E,  $<10\text{ ns}$ ,  $0.1\text{ cm}^{-1}$  full width at half maximum) which are simultaneously pumped by a single Nd:YAG laser (Spectra Physics GCR-290, 5–7 ns pulse). The first dye laser (operating with Coumarin 540A laser dye, pumped by the third harmonic of the Nd:YAG laser, and equipped with a  $\beta$ -BBO frequency-doubling crystal;  $2\omega$  output power  $\sim 250\ \mu\text{J}$ ) is tuned to a single rotational line of the  $F'\ ^2\Sigma^+ \leftarrow X\ ^2\Sigma^+$  transition. Due to unresolved spin structure, this apparently single  $N' \leftarrow N''$  rotational line terminates on two same parity  $J'=N'+\frac{1}{2}$  and  $J'=N'-\frac{1}{2}$  levels. The output of the second dye laser (typically operating with pyridine 1, pumped by the second harmonic of the Nd:YAG laser; output power  $\sim 40\text{--}50\text{ mJ/pulse}$ ), is focused into a hydrogen Raman shifter (250 psi  $\text{H}_2$ ; 30 cm path length) to generate infrared light for the second excitation step. The first-Stokes output of the Raman shifter is spatially separated from both the input pulse and second-Stokes and all anti-Stokes outputs using a Pellin–Broca prism and is directed into the vacuum chamber

using quartz 90° turning prisms. The second laser is swept in frequency across the appropriate energy region and populates Rydberg states that lie above the first ionization threshold and spontaneously autoionize. The two laser pulses are separated in time by approximately one pulse length to avoid unwanted multiphoton excitations and coherence effects, and the frequencies of the pump and probe laser pulses are each calibrated using simultaneously recorded high-temperature absorption spectra of molecular iodine.

The spectra analyzed in this experiment are shown in Fig. 1. Figure 1(a) shows an overview of the entire data set upon which this analysis is based. The ten spectra which comprise Fig. 1(a) each cover the same range of  $n^*$  but are recorded from different rotational levels of the  $F' \ ^2\Sigma^+$  intermediate state, and are stacked to aid in the identification of rotational branches. The rotational quantum number of the intermediate state  $N''$  is given on the left-hand side of each spectrum, and nonpenetrating Rydberg states are indicated by the Hund's case (d) labels  $\ell(\ell_R)^\pm$ . Figure 1(b) shows an expanded view of the region inside the box in Fig. 1(a) and Fig. 1(c) shows an expanded view of the region inside the box in Fig. 1(b).

## B. Polarization measurements

The assignment of spectra relies on the observation of spectral patterns. Since the angular momentum coupling case of nonpenetrating Rydberg states changes quite rapidly at low  $N$  from Hund's case (b) to Hund's case (d), it is sometimes difficult to recognize the spectroscopic patterns that are so typical of these limiting cases, and therefore it is also difficult to assign these states a definitive set of  $\{N, \ell, N^+\}$  quantum numbers. For the Rydberg states investigated here, this is particularly true when  $N < 5$ . To alleviate this difficulty and help confirm assignments of some transitions observed in the double-resonance spectra, particularly transitions terminating on Rydberg states with  $N < 5$ , a series of intensity measurements were made using pairs of circularly polarized laser pulses, using the techniques described in detail by Petrović and Field.<sup>9</sup>

The apparatus described in Sec. II A was slightly modified to perform these polarized excitation measurements. Linear polarizers were inserted into the path of both the pump and probe laser beams to improve the polarization contrast ratio of each output beam. The pump laser beam is then directed through a Soleil–Babinet polarizer to generate right-hand circularly polarized light. The probe laser beam is directed through a pair of Fresnel rhombs, which can be oriented to generate either right-hand circularly polarized light (same helicity as the pump beam) or left-hand circularly polarized light (helicity opposite to that of the pump beam).

In these measurements, the intensity of the double resonance signal using same-helicity pulses  $S$  is compared to the intensity of the signal measured using opposite-helicity pulses  $O$ . The ratio of the two signals  $S/O$  gives a strong indication of the change in total angular momentum  $\Delta N$  that occurs in the second excitation step for each transition in the double resonance spectrum. Since in these experiments the first transition ( $F' \ ^2\Sigma^+ \leftarrow X \ ^2\Sigma^+$ ) always involves  $R$ -type tran-

sition ( $\Delta N = +1$ ), an  $S/O$  ratio greater than unity indicates that the second transition is an  $R$ -type transition, an  $S/O$  ratio less than unity indicates that the second transition is a  $P$ -type transition ( $\Delta N = -1$ ), and an  $S/O$  ratio approximately equal to one is indicative of a  $Q$ -type transition ( $\Delta N = 0$ ). These polarization measurements therefore provide unambiguous assignment of  $N$  for each Rydberg state. When combined with information that can be extracted purely from the spectrum alone, as described below in Sec. III A, it is nearly always possible to assign a complete set of  $\{N, \ell, N^+\}$  quantum numbers to these particularly problematic Rydberg states.

## III. RESULTS AND DISCUSSION

### A. Assignment of spectra

All of the double resonance spectra were assigned using the techniques described in Ref. 8, but at low  $N$  these techniques were supplemented using the information provided by the above polarization measurements. We will briefly discuss the assignment strategies here.

Definite assignments of nonpenetrating Rydberg states are difficult because the states rapidly evolve from Hund's case (b) coupling toward Hund's case (d) coupling with increasing rotational excitation. Hund's case (b) coupling, which is typically observed in Rydberg states with low effective principal quantum number  $n^*$  and at low rotation (i.e., when the Born–Oppenheimer approximation is valid), is characterized by the presence of well-separated electronic states and regular  $BN(N+1)$  rotational energy level patterns. The rotational pattern-forming quantum number in case (b) is  $N$ , the total angular momentum of the molecule apart from spin, and the orbital angular momentum of the Rydberg electron  $\ell$  is quantized along the internuclear axis with projection  $\lambda$ . Hund's case (d) coupling, on the other hand, is typically observed in Rydberg states with high  $n^*$  and/or at high rotation, when the rotational energy level spacings become larger than the spacing between adjacent electronic states. The rotational pattern-forming quantum number in case (d) is  $N^+$ , the total angular momentum of the free ion, and the rotational energy is given by  $E_{\text{Rot}} = BN^+(N^++1)$ . The orbital angular momentum of the Rydberg electron is quantized along the axis of rotation, with projection  $\ell_R$ . The transition between the two coupling cases is driven by the “ $\ell$ -uncoupling” interaction,<sup>10</sup> which becomes stronger with increasing rotational excitation. This transition from one coupling case to another is accompanied by abrupt changes in the rotational energy level patterns, which makes the identification of rotational branches difficult.<sup>8,10,11</sup>

The unique assignment of nonpenetrating Rydberg states involves at the very least the determination of (i) the total angular momentum  $N$ , (ii) the orbital angular momentum  $\ell$ , and (iii) one of the remaining three quantum numbers: The projection of  $\ell$  along the internuclear axis  $\lambda$ , the projection of  $\ell$  along the axis of rotation  $\ell_R$ , or the total angular momentum of the free ion core,  $N^+$ . The total angular momentum of the molecule  $N$  is rigorously conserved and can be assigned using the method of combination differences, which involves comparing spectra recorded from adjacent rota-

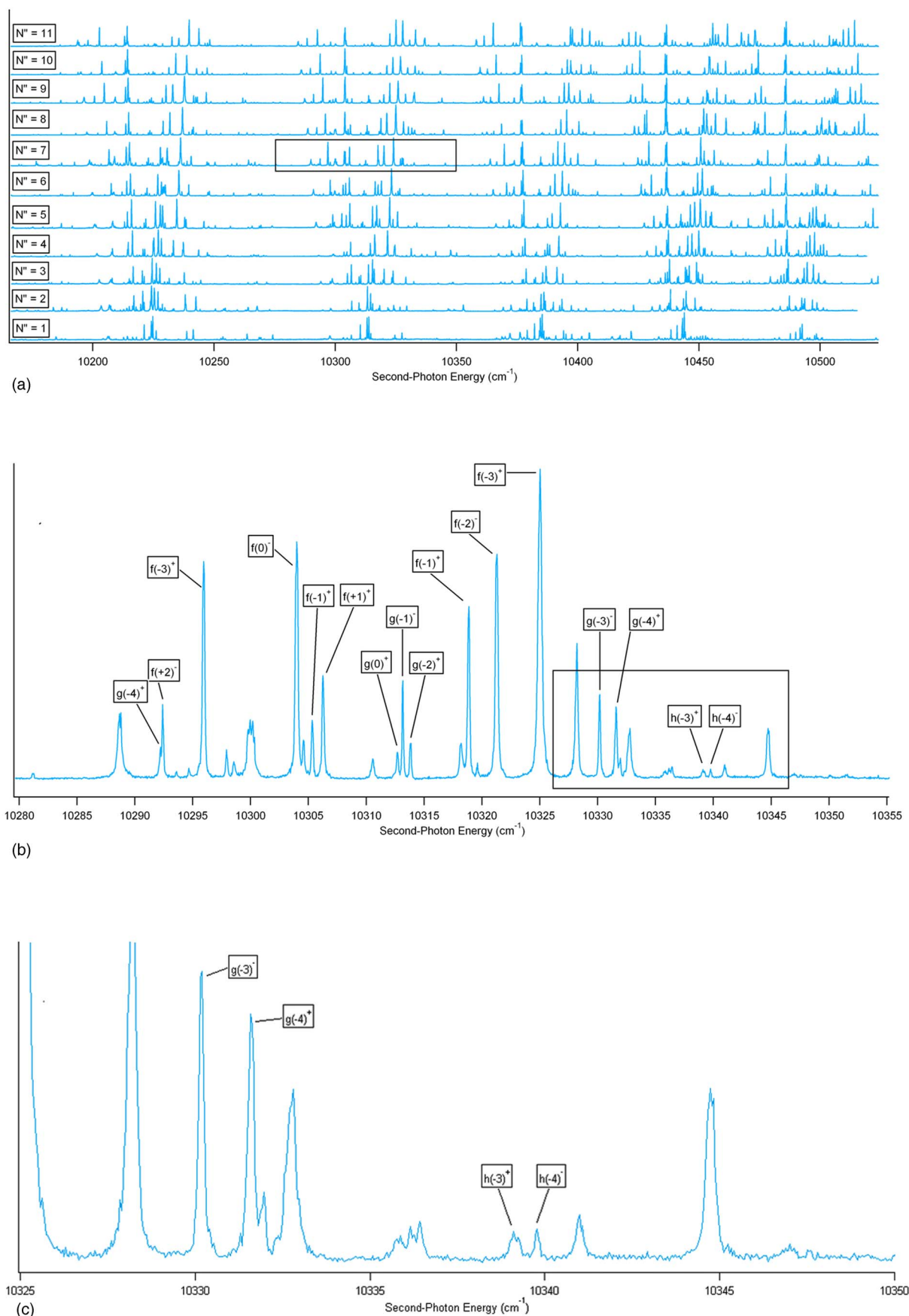


FIG. 1. (Color online) (a) Overview of the experimental spectra analyzed in this work. (b) Expanded view of boxed region in (a). (c) Expanded view of boxed region in (b). State labels are given in (b) and (c) using the Hund's case (d) labels  $\ell(\ell_R)^\pm$ .



TABLE I. Selection rules for operators relevant to the long-range model. “x” indicates that matrix elements are only nonzero when  $\Delta n \neq 0$ . “■” indicates that matrix elements are nonzero for all values of  $\Delta n$ . Blanks indicate that all matrix elements are zero for the specified value of  $\Delta \ell$ .

$\Delta \ell$	$r^{-2}$	$r^{-3}$	$r^{-4}$	$r^{-5}$	$r^{-6}$	$P_1(\cos \theta)$	$P_2(\cos \theta)$	$P_3(\cos \theta)$	$P_4(\cos \theta)$
0	■	■	■	■	■		■		■
$\pm 1$	x	■	■	■	■	■		■	
$\pm 2$	x	x	■	■	■		■		■
$\pm 3$	x	x	x	■	■			■	
$\pm 4$	x	x	x	x	■				■

tional levels of the  $F' \ ^2\Sigma^+$  intermediate in order to identify transitions to a common upper state.<sup>8,12</sup> Once  $N$  has been assigned, rotational levels are organized into branches and their reduced energies  $E_{\text{red}} = E - BN(N+1)$  are plotted against  $N$ . At high  $N$ , the slope of each branch on such a plot is approximately  $-2B\ell_R$ ,<sup>8,10</sup> and this determines both  $\ell_R$  and  $N^+$  simultaneously since  $\ell_R = N - N^+$ . This allows us to calculate for each rotational branch the quantity  $N^{+'} - N''$  (single prime refers to Rydberg states, double prime refers to the intermediate  $F' \ ^2\Sigma^+$  state), and since the parity of case (d) coupled Rydberg states  $p = (-1)^{\ell+N^+}$  alternates with  $\ell$ , only branches with even (odd)  $N^{+'} - N''$  and odd (even)  $\ell$  are observed in the spectrum. This gives rise to a spectral pattern in which rotational branches are staggered according to  $\ell$ ,<sup>8</sup> and permits  $\ell$  to be assigned by inspection. This completes the assignment process.

Levels with low  $N$  (typically,  $N < 5$ ), for which  $N$  is often difficult to assign on account of irregular level patterns and spectral congestion, were subject to the additional polarization measurements described in Sec. II B. These measurements provided additional information which allowed definite assignment of  $N$ , definite association of each such level into a rotational branch, and ultimately allowed rigorous assignments to be made in all cases.

A list of all energy levels assigned in this work can be found in Ref. 13.

## B. Basic long-range model for nonpenetrating states

The long-range model for nonpenetrating Rydberg states treats the nonpenetrating states of both atoms and molecules as hydrogenic eigenstates perturbed by long-range interactions with the ion core. The effective Hamiltonian, for both atoms and nonrotating molecules, may be written as

$$\hat{H} = \hat{H}_{\text{Coulomb}} + \hat{H}_{\text{el}}^{(1)}. \quad (1)$$

Here  $\hat{H}_{\text{el}}^{(1)}$  is the operator representing all non-Coulomb long-range interactions between the electron and ion and includes perturbations by the permanent electric multipole fields of the ion core as well as polarization of the core electron orbitals by the Rydberg electron. The electric multipole interactions, which are typically much stronger than the polarization interactions, are of the general form<sup>14</sup>

$$V(r, \theta, \phi) = \sum_{\ell=0}^{\infty} \sum_{m=-\ell}^{\ell} \sqrt{\frac{4\pi}{2\ell+1}} \frac{Y_{\ell m}(\theta, \phi)}{r^{\ell+1}} Q_{\ell m}. \quad (2)$$

In a diatomic molecule, the cylindrical symmetry forces all terms with  $m \neq 0$  to vanish, leaving

$$\begin{aligned} V(r, \theta, \phi) &= \sum_{\ell=0}^{\infty} \sqrt{\frac{4\pi}{2\ell+1}} \frac{Y_{\ell 0}(\theta, \phi)}{r^{\ell+1}} Q_{\ell 0} \\ &= \sum_{\ell=0}^{\infty} \sqrt{\frac{4\pi}{2\ell+1}} \frac{Y_{\ell 0}(\theta, \phi)}{r^{\ell+1}} Q_{\ell}, \end{aligned} \quad (3)$$

which may be written in terms of Legendre polynomials as

$$V(r, \theta) = \sum_{\ell=0}^{\infty} \frac{Q_{\ell}}{r^{\ell+1}} P_{\ell}(\cos \theta). \quad (4)$$

The  $\ell$ th moment  $Q_{\ell}$  is defined as

$$Q_{\ell} = \int dr' \rho(r') (r')^{\ell} P_{\ell}(\cos \theta), \quad (5)$$

where  $\rho(r')$  is the charge density of the core at point  $r'$ . Matrix elements of the electric multipole operators in Eq. (4) are evaluated in a hydrogenic basis,

$$\psi_{\ell m} = R_{n\ell}(r) Y_{\ell m}(\theta, \phi). \quad (6)$$

For diatomic molecules, the internuclear axis is taken as the axis of quantization, and the projection quantum number  $m$  is replaced by  $\lambda$ .

The selection rules on the electric multipole operators of Eq. (4), summarized in Table I, are such that all odd-multipole operators (dipole,  $\ell=1$ ; octupole,  $\ell=3$ ; etc.) have matrix elements that are exclusively off diagonal in the orbital angular momentum quantum number  $\ell$ . On the other hand, the even multipole operators (quadrupole,  $\ell=2$ ; hexadecapole,  $\ell=4$ ; etc.) contribute matrix elements that are both diagonal and off diagonal in  $\ell$ , and the off-diagonal matrix elements have a much weaker effect on the energy level structure. For homonuclear molecules, all odd electric multipole moments vanish by symmetry and therefore only the even multipole operators need be considered. Because the dominant interactions are diagonal in both  $\ell$  and  $n$ , the orbital basis set can usually be truncated to include only the set of  $2\ell+1$  substates with common values of  $\ell$  and  $n$ . For example, in NO (a near-homonuclear molecule) the  $\Delta n \neq 0$  and  $\Delta \ell \neq 0$  interactions are sufficiently weak that the  $4f$  states can effectively be treated as an isolated set of seven ( $4f\sigma^+$ ,

$4f\pi^\pm$ ,  $4f\delta^\pm$ , and  $4f\varphi^\pm$  sublevels.<sup>11</sup> In heteronuclear diatomics, all electric multipole moments are in principle nonzero. The presence of the odd-multipole fields can complicate the analysis considerably, especially when one of the odd moments is large. The analysis is significantly more complicated in the heteronuclear case because the  $\Delta n \neq 0$  and  $\Delta \ell \neq 0$  interactions cannot be neglected, and the orbital basis must be expanded significantly.

Watson<sup>5</sup> devised a perturbation-theoretic scheme to cope with the presence of a large dipole moment. Because the dipole operator has exclusively off-diagonal elements (selection rule  $\Delta \ell = \pm 1$ ), the first-order correction to the energy levels in the perturbation expansion

$$\begin{aligned} E_{n\ell\lambda} &= E_{n\ell}^{(0)} + E_{n\ell\lambda}^{(1)} + E_{n\ell\lambda}^{(2)} + \cdots \\ &= E_{n\ell}^{(0)} + \langle \psi_{n\ell\lambda}^{(0)} | V(r) | \psi_{n\ell\lambda}^{(0)} \rangle \\ &\quad + \sum_{n'\ell'} \frac{|\langle \psi_{n'\ell'}^{(0)} | V(r) | \psi_{n\ell\lambda}^{(0)} \rangle|^2}{E_{n'\ell'}^{(0)} - E_{n\ell}^{(0)}} + \cdots \end{aligned} \quad (7)$$

vanishes. However, the second-order correction is nonzero and, according to Watson's formalism, has the value

$$E_{n\ell\lambda}^{(2)} = \mu^2 \frac{2[\ell(\ell+1) - 3\lambda^2]}{n^3(2\ell+3)(2\ell+1)(2\ell-1)\ell(\ell+1)}. \quad (8)$$

The utility of Watson's approach is that it allows the effects of an infinite number of interactions among an infinite number of energy levels to be calculated using a closed-form expression, and more importantly, no expansion of the basis (beyond the usual  $2\ell+1$  substates typically employed for homonuclear molecules) is necessary. Because it is a pertur-

bative method, it is not exact, but the error is typically only significant when  $\ell < 3$  and  $\mu > 3$  a.u.

For both homonuclear and heteronuclear molecules, evaluation of the matrix elements of even multipole operators is quite simple. The first-order diagonal matrix elements are<sup>15-17</sup>

$$\begin{aligned} \langle \psi_{n\ell\lambda} | V_{\ell'}(r) | \psi_{n\ell\lambda} \rangle &= \left\langle R_{n\ell} \left| \frac{1}{r^{\ell'+1}} \right| R_{n\ell} \right\rangle \sqrt{\frac{4\pi}{2\ell+1}} \langle Y_{\ell\lambda} | Y_{\ell'0} | Y_{\ell\lambda} \rangle \\ &= \left\langle R_{n\ell} \left| \frac{1}{r^{\ell'+1}} \right| R_{n\ell} \right\rangle \langle Y_{\ell\lambda} | C_0^k | Y_{\ell\lambda} \rangle, \end{aligned} \quad (9)$$

in which  $k \equiv \ell'$  and

$$\langle Y_{\ell\lambda} | C_q^k | Y_{\ell\lambda} \rangle = (-1)^{\ell-\lambda} \begin{pmatrix} \ell & k & \ell \\ -\lambda & q & \lambda \end{pmatrix} \langle \ell \| C(k) \| \ell \rangle. \quad (10)$$

The reduced matrix elements  $\langle \ell \| C(k) \| \ell \rangle$  are

$$\langle \ell \| C(k) \| \ell \rangle = (-1)^\ell (2\ell+1) \begin{pmatrix} \ell & k & \ell \\ 0 & 0 & 0 \end{pmatrix}. \quad (11)$$

The final matrix element for the first-order quadrupole interaction is

$$\langle \psi_{n\ell\lambda} | V_{\ell=2}(r) | \psi_{n\ell\lambda} \rangle = Q \frac{2[\ell(\ell+1) - 3\lambda^2]}{n^3(2\ell+3)(2\ell+1)(2\ell-1)\ell(\ell+1)} \quad (12)$$

and the final matrix element for the first-order hexadecapole interaction is

$$\langle \psi_{n\ell\lambda} | V_{\ell=4}(r) | \psi_{n\ell\lambda} \rangle = H \frac{3[5n^2 - 3\ell(\ell+1) + 1][\ell(\ell+1) - 2]}{[n^5(\ell+2)(\ell+\frac{3}{2})(\ell+1)\ell(\ell-1/2)(\ell-1)]} \frac{\{35\lambda^4 + 5[5 - 6\ell(\ell+1)]\lambda^2 + 3[\ell^2(\ell+1)^2 - 2\ell(\ell+1)]\}}{[(2\ell+5)(2\ell+4)(2\ell+3)(2\ell+1)(2\ell-1)(2\ell-2)(2\ell-3)]}. \quad (13)$$

The similarity between the first-order quadrupole matrix elements of Eq. (12) and the second-order dipole matrix elements of Eq. (8) is a general result: Odd-multipole operators operating in second order effectively behave as even multipole operators operating in first order.

In addition to perturbations by the permanent electric multipole moments of the core, the polarization of the core by the Rydberg electron must also be considered.<sup>2</sup> In lowest order, the polarization interactions give rise to a scalar term (the "isotropic polarization" or "scalar dipole polarization" interaction) and a second-rank tensor term (the "anisotropic polarization" or "tensor dipole polarization" interaction), which for cylindrically symmetric molecules have the forms

$$V_{\text{iso}}^{(D)}(r) = -\frac{1}{2} \frac{\alpha}{r^4} \quad (14)$$

and

$$V_{\text{aniso}}^{(D)}(r, \theta) = -\frac{1}{3} \frac{\gamma}{r^4} P_2(\cos \theta), \quad (15)$$

and their matrix elements are

$$\langle \psi_{n\ell\lambda} | V_{\text{iso}}^{(D)} | \psi_{n\ell\lambda} \rangle = \alpha \frac{2(\ell(\ell+1) - 3n^2)}{n^5(2\ell+3)(2\ell+1)(2\ell-1)\ell(\ell+1)} \quad (16)$$

and

$$\begin{aligned} \langle \psi_{n\ell\lambda} | V_{\text{aniso}}^{(D)} | \psi_{n\ell\lambda} \rangle &= \gamma \frac{4(\ell(\ell+1) - 3n^2)}{3n^5(2\ell+3)^2(2\ell+1)(2\ell-1)^2\ell(\ell+1)} \\ &\quad \times \{\ell(\ell+1) - 3\lambda^2\}. \end{aligned} \quad (17)$$

The isotropic polarizability  $\alpha$  and anisotropic polarizability  $\gamma$

are defined in terms of the components of the polarizability tensor as

$$\alpha = \frac{(2a_{\perp} + a_{\parallel})}{3} \quad (18)$$

and

$$\gamma = a_{\parallel} - a_{\perp}, \quad (19)$$

in which  $a_{\parallel} = a_{zz}$  is the polarizability of the core along a direction parallel to the internuclear axis, and  $a_{\perp} = a_{xx} = a_{yy}$  is the polarizability of the core perpendicular to the internuclear axis.

So far we have only considered the electrostatic part of the Hamiltonian. To incorporate the effects of molecular rotation, we must augment the Hamiltonian of Eq. (1) to include the rotational Hamiltonian of the molecule,

$$\hat{H} = \hat{H}_{\text{Coulomb}} + \hat{H}_{\text{el}} + \hat{H}_{\text{rot}}. \quad (20)$$

Neglecting electron and nuclear spin, the rigorously good rotational quantum number is  $N$ , where  $\mathbf{N} = \mathbf{J} - \mathbf{S}$  and  $N(N+1)$  are the eigenvalues of  $\mathbf{N}^2$ . The rotational Hamiltonian becomes<sup>10</sup>

$$\hat{H}_{\text{rot}} = B(R)[\mathbf{N}^2 + \ell^2 - 2\mathbf{N}_z \ell_z - \mathbf{N}^+ \ell^- - \mathbf{N}^- \ell^+]. \quad (21)$$

The first three terms in Eq. (21) are diagonal in  $N$ ,  $\ell$ , and  $\lambda$  with matrix elements

$$\langle N\ell\lambda | \hat{H}_{\text{rot}} | N\ell\lambda \rangle = E_{\text{rot}}^{(0)} = B[N(N+1) + \ell(\ell+1) - 2\lambda^2], \quad (22)$$

while the fourth and fifth terms (the “ $\ell$ -uncoupling” operators) are diagonal in  $N$  and  $\ell$  but off diagonal in  $\lambda$  (selection rule  $\Delta\lambda = \pm 1$ ), with matrix elements

$$\begin{aligned} \langle N\ell\lambda | \hat{H}_{\text{rot}} | N\ell\lambda \pm 1 \rangle \\ = -B(R)\sqrt{N(N+1) - \lambda(\lambda \pm 1)}\sqrt{\ell(\ell+1) - \lambda(\lambda \pm 1)} \cdot F. \end{aligned} \quad (23)$$

Here,  $F$  is a symmetry factor arising from the degeneracy of  $\Lambda^+$  and  $\Lambda^-$  substates, and has the value  $F = \frac{1}{2}$  when  $\lambda = 0$  or  $\lambda' = 0$  and  $F = 1$  otherwise.

Watson also notes<sup>5</sup> that the electric dipole operator also has second-order effects on some matrix elements in the rotational Hamiltonian. In the absence of a dipole field, the matrix elements of  $\ell^2$ ,  $\ell^+$ , and  $\ell^-$  are

$$\langle \psi_{n\ell\lambda \pm 1} | \ell^2 | \psi_{n\ell\lambda} \rangle^{(0)} = \ell(\ell+1). \quad (24)$$

$$\langle \psi_{n\ell\lambda \pm 1} | \ell^{\pm} | \psi_{n\ell\lambda} \rangle^{(0)} = \sqrt{\ell(\ell+1) - \lambda(\lambda \pm 1)}. \quad (25)$$

When the dipole moment is nonzero, an additional second-order contribution arises

$$\langle \psi_{n\ell\lambda \pm 1} | \ell^2 | \psi_{n\ell\lambda} \rangle^{(2)} = -\frac{\mu^2}{2\ell^2(\ell+1)^2}\ell(\ell+1), \quad (26)$$

$$\langle \psi_{n\ell\lambda \pm 1} | \ell^{\pm} | \psi_{n\ell\lambda} \rangle^{(2)} = -\frac{\mu^2}{2\ell^2(\ell+1)^2}\sqrt{\ell(\ell+1) - \lambda(\lambda \pm 1)}, \quad (27)$$

and the matrix elements of  $\ell^2$ ,  $\ell^+$ , and  $\ell^-$  therefore become

$$\langle \psi_{n\ell\lambda \pm 1} | \ell^2 | \psi_{n\ell\lambda} \rangle = \left[ 1 - \frac{\mu^2}{2\ell^2(\ell+1)^2} \right] \ell(\ell+1). \quad (28)$$

$$\langle \psi_{n\ell\lambda \pm 1} | \ell^{\pm} | \psi_{n\ell\lambda} \rangle = \left[ 1 - \frac{\mu^2}{2\ell^2(\ell+1)^2} \right] \sqrt{\ell(\ell+1) - \lambda(\lambda \pm 1)}. \quad (29)$$

The net effect of a nonzero dipole field is therefore to reduce the value of the matrix elements of  $\ell^2$ ,  $\ell^+$ , and  $\ell^-$  by a subtractive quantity which is multiplicatively proportional to  $\mu^2$ . Watson refers to this effect as “orbit-rotation drag,” and its physical interpretation is that the dipole field reduces the rate by which  $\ell$  is decoupled from the internuclear axis. Classically, the core dipole exerts a “drag” force on the Rydberg electron, which opposes the Coriolis force caused by molecular rotation. Quantum mechanically, the  $\Delta\ell = \pm 1$  mixing of the orbital angular momentum  $\ell$  is stronger for  $\Delta\ell = -1$  than it is for  $\Delta\ell = +1$ , effectively reducing the value of  $\ell$  to an effective noninteger value  $\ell^* < \ell$ .

### C. Extended long-range model for nonpenetrating states

Preliminary analysis of the nonpenetrating states identified in this study indicate that the long-range model described in Sec. III B does not adequately describe the energy level structure of the  $nf$  states of CaF. We have therefore augmented the long-range model to include the effects of higher-order multipole fields. Since  $\text{CaF}^+$  is extremely polar, it is reasonable to expect that the higher-order electric multipole fields could have a measurable impact on the energy level structure, and preliminary calculations indeed indicated that the octupole field might give rise to as much as 5%  $d \sim f$  mixing. However, the matrix elements of the next highest polarization term, the adiabatic quadrupole polarization interaction,

$$V_{\text{Pol}}^{(Q)}(r, \theta) = -\frac{1}{r^6} \left( \frac{\chi_0}{10} + \frac{\chi_2}{7} P_2(\cos \theta) + \frac{12\chi_4}{35} P_4(\cos \theta) \right) \quad (30)$$

should be weaker by a factor of at least 70 for  $13f$ , even if the magnitude of the adiabatic quadrupole polarizability were equal to the magnitude of the adiabatic dipole polarizability. If that were the case, the quadrupole polarizability term would contribute energy level shifts that are significantly below our sensitivity limit of  $\sim 0.05 \text{ cm}^{-1}$ . We therefore restrict our attention to the higher-order permanent electric multipole operators.

To develop expressions for the matrix elements of the higher-order multipole interactions, we first note that the second-order term in the perturbation expansion of Eq. (7),

$$E_{n\ell}^{(2)} = \sum_{n'\ell'} \frac{|\langle \psi_{n'\ell'\lambda}^{(0)} | V(r) | \psi_{n\ell\lambda}^{(0)} \rangle|^2}{E_{n'\ell'}^{(0)} - E_{n\ell}^{(0)}} \quad (31)$$

contains a square in the numerator, which gives rise to cross terms between the terms in the electric multipole expansion

$$V(r, \theta) = -\frac{\mu}{r^2} P_1(\cos \theta) - \frac{Q}{r^3} P_2(\cos \theta) - \frac{O}{r^4} P_3(\cos \theta) - \frac{H}{r^5} P_4(\cos \theta) \cdots \quad (32)$$

Cross terms between even and odd-multipole moments vanish on account of parity, and the only cross terms that remain are those with overall positive parity. The nonzero second-order cross terms are

$$V_{11}(r, \theta) = \frac{\mu}{r^2} P_1(\cos \theta) \frac{\mu}{r^2} P_1(\cos \theta), \quad (33)$$

$$V_{22}(r, \theta) = \frac{Q}{r^3} P_2(\cos \theta) \frac{Q}{r^3} P_2(\cos \theta), \quad (34)$$

$$V_{33}(r, \theta) = \frac{O}{r^4} P_3(\cos \theta) \frac{O}{r^4} P_3(\cos \theta), \quad (35)$$

and

$$V_{13}(r, \theta) = \frac{\mu}{r^2} P_1(\cos \theta) \frac{O}{r^4} P_3(\cos \theta). \quad (36)$$

In the above, the subscripts on  $V$  stand for  $\ell$  and  $\ell'$ , respectively; for example,  $V_{13} \equiv V_{\ell=1, \ell'=3}$ . The matrix elements in Eqs. (33)–(36) represent the second-order dipole, second-order quadrupole, second-order octupole, and second-order dipole-octupole interactions.

To calculate the matrix elements of these operators we use the effective operator method developed by Kazansky and Ostrovsky.<sup>18,19</sup> In their method, the traditional perturbation sum in Eq. (7) is replaced by a Green's function

$$E_{n\ell\lambda} = E_{n\ell}^{(0)} + \langle \psi_{n\ell\lambda}^{(0)} | V | \psi_{n\ell\lambda}^{(0)} \rangle + \langle \psi_{n'\ell'\lambda}^{(0)} | V \tilde{G}(E) V | \psi_{n\ell\lambda}^{(0)} \rangle + \cdots, \quad (37)$$

and the effect of the Green's functions is expressed in terms of an effective tensor operator  $\hat{W}$ ,

$$\langle \psi_{n'\ell'\lambda}^{(0)} | (A_{k1} V_{k1}) \tilde{G}(E) (A_{k2} V_{k2}) | \psi_{n\ell\lambda}^{(0)} \rangle = \langle \psi_{n'\ell'\lambda}^{(0)} | \hat{W} | \psi_{n\ell\lambda}^{(0)} \rangle. \quad (38)$$

The  $V_{\kappa_1}$  represent the individual terms of the multipole expansion and the  $A_{\kappa_1}$  represent their coefficients, for example  $A_2 V_2 = -(Q/r^3) P_2(\cos \theta)$  is the quadrupole term. The operator  $\hat{W}$  is itself a sum of  $\ell+1$  tensor operators  $\hat{W}_{kq}$ ,

$$\hat{W} = \sum_{k,q} A_{kq} \hat{W}_{kq}. \quad (39)$$

The rank of the effective operator  $W_{kq}$  is given by  $k$  and the components of the tensor are indexed by  $q$ . The effective moment  $A_{kq}$  of each effective tensor operator  $W_{kq}$  is given by the tensor product of the coefficients of the electric multipole moment comprising the cross term,

$$A_{kq} = (A_{\kappa_1} \otimes A_{\kappa_2})_{kq}, \quad (40)$$

in which

$$(A_{\kappa_1} \otimes A_{\kappa_2})_{kq} = C_{\kappa_1 q_1, \kappa_2 q_2}^{k,q}. \quad (41)$$

Here,  $C_{\kappa_1 q_1, \kappa_2 q_2}^{k,q}$  is the Clebsch–Gordan coefficient  $\langle \kappa_1 q_1, \kappa_2 q_2 | \kappa, k, q \rangle$ , and  $\kappa_1$  and  $\kappa_2$  represent the orders of the two multipole terms comprising the cross-term ( $\kappa=1$  for the dipole term,  $\kappa=2$  for the quadrupole term, etc.). The sum in Eq. (39) therefore extends over all combinations of  $\kappa_1$  and  $\kappa_2$  for which  $C_{\kappa_1 q_1, \kappa_2 q_2}^{k,q} \neq 0$ . The effective tensor operators  $W_{kq}$  are expressed in terms of reduced matrix elements  $\langle \ell_1 || W_k || \ell_3 \rangle$ , just as in Eq. (10),

$$\langle \psi_{n'\ell'\lambda}^{(0)} | W_{kq} | \psi_{n\ell\lambda}^{(0)} \rangle = (-1)^{\ell_1 - \lambda_1} \begin{pmatrix} \ell_1 & k & \ell_3 \\ -\lambda_1 & q & \lambda_3 \end{pmatrix} \langle \ell_1 || W_k || \ell_3 \rangle. \quad (42)$$

The reduced matrix elements  $\langle \ell_1 || W_k || \ell_3 \rangle$  consist of products of radial and angular terms,

$$\langle \ell_1 || W_k || \ell_3 \rangle = \sum_{\ell_2} \langle \ell_1 || w_k^{\ell_2} || \ell_3 \rangle \langle R_{n\ell_1} | \nu_{\kappa_1} \tilde{g}_{\ell_2} \nu_{\kappa_2} | R_{n\ell_3} \rangle, \quad (43)$$

and the angular portion is given by

$$\begin{aligned} \langle \ell_1 || w_k^{\ell_2} || \ell_3 \rangle &= (-1)^{\ell_2 + \ell_3 + k} (2\ell_2 + 1) \\ &\times \sqrt{(2\ell_1 + 1)(2\ell_3 + 1)(2k + 1)} \\ &\times \begin{pmatrix} \ell_1 & \kappa_1 & \ell_2 \\ 0 & 0 & 0 \end{pmatrix} \begin{pmatrix} \ell_2 & \kappa_2 & \ell_3 \\ 0 & 0 & 0 \end{pmatrix} \begin{Bmatrix} \kappa_1 & \kappa_2 & k \\ \ell_3 & \ell_1 & \ell_2 \end{Bmatrix}. \end{aligned} \quad (44)$$

Here,  $\kappa_1$  and  $\kappa_2$  again represent the orders of the two multipole terms comprising the cross term, as in Eq. (40). The radial matrix elements  $\langle R_{n\ell_1} | \nu_{\kappa_1} \tilde{g}_{\ell_2} \nu_{\kappa_2} | R_{n\ell_3} \rangle$  are expressed in terms of a reduced Green's function  $\tilde{g}_{\ell_2}$  and may be generated by recursion.

The recursive generation of the matrix elements  $\langle R_{n\ell_1} | \nu_{\kappa_1} \tilde{g}_{\ell_2} \nu_{\kappa_2} | R_{n\ell_3} \rangle$  is based on the fact that the hydrogenic radial wavefunctions  $R_{n\ell}(r)$  may be expressed in terms of spherical Bessel functions,



$$R_{n\ell}(r) = \frac{\sqrt{2}}{n^{3/2}} \frac{1}{\sqrt{r}} J_{2\lambda+1}[\sqrt{8r}], \quad (45)$$

for which a recursion relationship exists:

$$\frac{1}{\sqrt{8r}} J_{2\lambda+1}[\sqrt{8r}] = \frac{1}{2(2\lambda+1)} (J_{2\lambda}[\sqrt{8r}] + J_{2\lambda+2}[\sqrt{8r}]). \quad (46)$$

Here, the correspondence between the subscript of the Bessel function,  $t = \dots, 2\lambda-2, 2\lambda-1, 2\lambda, 2\lambda+1, 2\lambda+2, \dots$ , is related to the orbital angular momentum quantum number  $\ell$  through the relationship  $t/2 = \ell$ . Equations (45) and (46) may be combined to give

$$\begin{aligned} \frac{1}{r} R_{n\ell} = \frac{1}{\sqrt{2}(\ell + \frac{1}{2})} & \left\{ \frac{1}{\ell\sqrt{2}} (R_{n\ell-1} + R_{n\ell}) \right. \\ & \left. + \frac{1}{\sqrt{2}(\ell+1)} (R_{n\ell} + R_{n\ell+1}) \right\}. \end{aligned} \quad (47)$$

Kazansky and Ostrovsky explicitly give the effective second-order dipole radial matrix element as

$$\begin{aligned} & \left\langle R_{n\ell_1} \left| \frac{1}{r^2} g_{\ell_2} \frac{1}{r^2} \right| R_{n\ell_3} \right\rangle \\ &= \frac{2}{\pi n^3} \frac{1}{(\ell_2 - \ell_3)(\ell_1 - \ell_2)(\ell_1 + \ell_2 + 1)(\ell_2 + \ell_3 + 1)} \\ & \times \left\{ \frac{(2\ell_1 + 1)^2 + (2\ell_3 + 1)^2 - 2(2\ell_2 + 1)^2}{4(\ell_1 - \ell_3)(\ell_1 - \ell_3 + 1)} \right. \\ & \times \left. \sin[\pi(\ell_1 - \ell_3)] - \sin[\pi(\ell_1 + \ell_3 - 2\ell_2)] \right\}. \end{aligned} \quad (48)$$

Using this matrix element it is possible to generate matrix elements for any of the cross terms in the multipole expansion. It should be noted that Eq. (48) has many removable singularities and must be explicitly evaluated for all possible values of the three angular momenta. Limits must be taken when two of the angular momenta are equal, and it will generally be found that the appearance of  $\sin x/x$  functions remove the singularities under such circumstances. Equations (47) and (48) may be combined to give the recurrence relationship,

$$\begin{aligned} & \left\langle R_{n\ell_1} \left| \frac{1}{r^{\kappa_1-1}} g_{\ell_2} \frac{1}{r^{\kappa_2-1}} \right| R_{n\ell_3} \right\rangle \\ &= [\langle R_{n\ell_1} | \hat{D}_1^{2\kappa_1-2} | R_{n\ell_3} \rangle] \frac{1}{r^2} g_{\ell_2} \frac{1}{r^2} [\hat{D}_3^{2\kappa_2-2} | R_{n\ell_3} \rangle]. \end{aligned} \quad (49)$$

The operator  $\hat{D}_1$  acts  $2\kappa_1-2$  times on the left and the operator  $\hat{D}_3$  acts  $2\kappa_2-2$  times on the right. The operators  $\hat{D}_i$  are defined as

$$\hat{D}_i[R_{n\ell_i}] = \frac{1}{\sqrt{2}(\ell_i + 1/2)} (R_{n,\ell_i+1/2} + R_{n,\ell_i-1/2}). \quad (50)$$

The final contributions are, for the second-order dipole interaction, effective matrix elements of rank 0 and 2,

$$\langle \psi_{n\ell\lambda} | V_{11} | \psi_{n\ell\lambda} \rangle^{(2,k=0)} = 0, \quad (51)$$

$$\begin{aligned} & \langle \psi_{n\ell\lambda} | V_{11} | \psi_{n\ell\lambda} \rangle^{(2,k=2)} \\ &= \mu^2 \frac{2\{\ell(\ell+1) - 3\lambda^2\}}{n^3(2\ell+3)(2\ell+1)(2\ell-1)\ell(\ell+1)}. \end{aligned} \quad (52)$$

The electric quadrupole moment in second order contributes to matrix elements of ranks 0, 2, and 4,

$$\begin{aligned} & \langle \psi_{n\ell\lambda} | V_{22} | \psi_{n\ell\lambda} \rangle^{(2,k=0)} \\ &= Q^2 \frac{2(40\ell^4 + 80\ell^3 + 30\ell^2 - 10\ell - 3)}{3n^3(2\ell+3)^2(2\ell+1)^3(2\ell-1)^2\ell^2(\ell+1)^2}, \end{aligned} \quad (53)$$

$$\langle \psi_{n\ell\lambda} | V_{22} | \psi_{n\ell\lambda} \rangle^{(2,k=2)} = Q^2 \frac{10(560\ell^6 + 1680\ell^5 - 840\ell^4 - 1120\ell^3 - 777\ell^2 + 63\ell + 45)}{21n^3(2\ell+3)^3(2\ell+1)^3(2\ell-1)^3\ell^3(\ell+1)^3} \{\ell(\ell+1) - 3\lambda^2\}, \quad (54)$$

$$\begin{aligned} & \langle \psi_{n\ell\lambda} | V_{22} | \psi_{n\ell\lambda} \rangle^{(2,k=4)} = \frac{Q^2}{7n^3} (560\ell^8 + 2240\ell^7 - 7000\ell^6 - 28840\ell^5 - 19537\ell^4 + 11606\ell^3 + 10497\ell^2 - 486\ell - 540) \\ & \times ((2\ell+5)(2\ell+3)^3(2\ell+1)^3(2\ell-1)^3(2\ell-3)\ell^3(\ell+1)^3(\ell-1)(\ell+2))^{-1} \\ & \times \{35\lambda^4 - 5(6\ell(\ell+1) - 5)\lambda^2 + 3(\ell+2)(\ell-1)\ell(\ell+1)\}. \end{aligned} \quad (55)$$

The second-order dipole-octupole cross term contributes effective matrix elements of ranks 2 and 4, and the second-order octupole interaction generates effective matrix elements of ranks 0, 2, 4, and 6. The expressions for these effective matrix elements are given in Appendix A. Note that the equation for the second-order electric dipole matrix element derived using this method, Eq. (52), is exactly equal to the matrix element derived by Watson, given in Eq. (8).

A full account of higher-order polarization interactions has been given in a long series of papers by Lundeen and co-workers,<sup>20–28</sup> and for a description of these polarization terms we refer interested readers to those documents.

$$\begin{aligned}
 E_{n\ell\lambda} = & \frac{C^{(0)}}{n^3} + \frac{C^{(2)}}{n^3} \{ \ell(\ell+1) - 3\lambda^2 \} + \frac{C^{(4)}}{n^3} \{ 35\lambda^4 - 5(6\ell(\ell+1) - 5)\lambda^2 + 3(\ell+2)(\ell-1)\ell(\ell+1) \} \\
 & + \frac{C^{(6)}}{n^3} \{ 5\ell^2(63\lambda^4 + 84\lambda^2 + 4) + 15\ell(21\lambda^4 + 35\lambda^2 + 4) - 21\lambda^2(11\lambda^4 + 35\lambda^2 + 14) - 5\ell^4(21\lambda^2 + 5) - 15\ell^3(14\lambda^2 + 5) \\
 & + 5\ell^6 + 15\ell^5 \} + \eta \cdot B [N(N+1) + \ell(\ell+1) - 2\lambda^2]
 \end{aligned} \quad (56)$$

and off-diagonal elements

$$\begin{aligned}
 \langle N\ell\lambda | \hat{H}_{\text{rot}} | N\ell\lambda \pm 1 \rangle \\
 = -\eta \cdot B \sqrt{N(N+1) - \lambda(\lambda \pm 1)} \sqrt{\ell(\ell+1) - \lambda(\lambda \pm 1)} \cdot F.
 \end{aligned} \quad (57)$$

Here, we expand on the analysis of Dabrowski *et al.*<sup>29–33</sup> to include multipole moments beyond the electric quadrupole moment.

Assuming that the rotational constant of the ion core  $B$  is known with sufficient accuracy, the Hamiltonian described above has five adjustable parameters: The four tensor coefficients  $C^{(0)}$ ,  $C^{(2)}$ ,  $C^{(4)}$ , and  $C^{(6)}$  which arise from the electrostatic interactions, and one parameter  $\eta$  which arises from rotation-electronic interactions. After fitting the data to this expansion, each tensor coefficient resulting from the fit is equated with a sum of all nonzero matrix elements of a common tensor rank. This gives a system of equations which can be solved to determine the multipole moments and polarizabilities.

The most important consideration in this respect is to ensure that the multipole moments and polarizabilities can be separated using the data at hand. This can be difficult because the adiabatic dipole and quadrupole polarization operators have the same angular dependence as the electric dipole and quadrupole operators, and therefore in general their effects cannot be separated from one another by a fit to a set of data in which only one value of  $\ell$  is represented. The radial parts of the matrix elements are different, however, and this gives their matrix elements a dramatically different dependence on  $\ell$  and a mildly different dependence on  $n$ . The separation of multipole moments and polarizabilities can therefore either be accomplished through (i) a simultaneous

#### D. General scheme for determination of multipole moments and separation of long- and short-range interactions in diatomic molecules

Using the above analysis, it is possible to separately and precisely determine the value of each of the multipole moments and polarizabilities for any molecule, given sufficient sensitivity of the data in question. As Dabrowski *et al.*<sup>29–33</sup> have shown, the most straightforward way to accomplish this is to fit the energy levels directly to a tensor expansion of an effective Hamiltonian with diagonal matrix elements

fit of Rydberg states with different values of the orbital angular momentum  $\ell$  (for example, a simultaneous fit of all components of  $10f$  and  $10g$ ) or (ii) by simultaneously fitting states with identical  $\ell$  but spanning a wide range of  $n$  (for example, fitting all states with  $\ell=3$  and  $5 < n < 15$ ).

Assuming that the data in question span at least two values of  $\ell$  or a wide range of  $n$ , there should be at least as many equations as unknown variables in the relevant set of simultaneous equations. In general, at a laser resolution of between  $0.03 \text{ cm}^{-1}$  (typical for high-resolution nanosecond pulsed lasers) and  $0.001 \text{ cm}^{-1}$  (typical for pulse-amplified continuous-wave lasers), the tensor coefficients should be sensitive to the isotropic polarizability, anisotropic polarizability, the electric dipole moment, the electric quadrupole moment, and the electric octupole moment for  $f$  states and the isotropic polarizability, anisotropic polarizability, the electric dipole moment and the electric quadrupole moment for  $g$  states. This would provide approximately six measurable tensor coefficients and two measurable orbit-rotation drag parameters, a total of approximately eight equations in exactly six unknowns, and the set of equations should in principle be soluble.

It should be emphasized that the orbit-rotation drag parameter of Eqs. (28) and (29),

$$\eta = \left[ 1 - \frac{\mu^2}{2\ell^2(\ell+1)^2} \right], \quad (58)$$

in principle allows separation of the electric dipole and quadrupole moments, which contribute to the second-rank tensor coefficients with identical  $\ell$  and  $n$  dependencies.

TABLE II. Calculated values of the static electric multipole moments of CaF. All quantities are in atomic units ( $e \cdot a_0^n$ , where  $e$  is the elementary charge and  $a_0$  is the Bohr radius), as given in parentheses in the first column.

Moment	Point-charge model	One-electron <i>ab initio</i>	All-electron <i>ab initio</i>
Monopole ( $e$ )	1.00	1.00	1.00
Dipole ( $e \cdot a_0$ )	-4.68	-3.47	-3.36
Quadrupole ( $e \cdot a_0^2$ )	-3.15	-0.15	-0.87
Octupole ( $e \cdot a_0^3$ )	-16.78	-1.18	-5.0
Hexadecapole ( $e \cdot a_0^4$ )	-29.76	12.89	-7.0

### E. Calculation of CaF<sup>+</sup> electric multipole moments and polarizabilities by *ab initio* methods

To support the spectroscopic analysis presented in this investigation, we have calculated the CaF<sup>+</sup> multipole moments and polarizabilities using a variety of computational methods. Specifically, these quantities have been calculated using (i) the point-charge model, which sets an upper bound on the magnitudes of the CaF<sup>+</sup> electric multipole moments, (ii) calculations using an *ab initio* one-electron effective potential for the CaF<sup>+</sup> core,<sup>34</sup> and (iii) new all-electron *ab initio* calculations, which explicitly consider interactions among all of the core electrons and are expected to provide the most accurate estimates of the core multipole moments and polarizabilities.

The simplest among these is the point-charge model, which treats the Ca<sup>2+</sup> and F<sup>-</sup> ions that constitute the CaF<sup>+</sup> core as a pair of point charges separated by the equilibrium internuclear distance,  $R_e^+ = 3.54 a_0$ . The charge distribution of the core is therefore discrete, and the integral of Eq. (5) is replaced by a sum. The multipole moments are calculated according to

$$Q_\ell = \sum_i q_i (z_i)^\ell, \quad (59)$$

where  $q_i$  is the charge on particle  $i$  (+2 for Ca<sup>2+</sup> and -1 for F<sup>-</sup>) and  $z_i$  is the (signed) distance between particle  $i$  and the center of mass of the system. The electric multipole moments calculated using this method are shown in the first column of Table II. While this model clearly constitutes an unrealistic oversimplification of the problem, it provides useful information in the sense that it sets a rigorous upper bound on the core dipole moment and, as we will see below, overestimates the magnitudes of the other electric multipole moments. The fact that the point-charge model *overestimates* the values of the higher moments will provide considerable leverage for the arguments presented in Secs. III F–III H.

The effective one-electron *ab initio* calculations are based on the potential developed by Arif *et al.*,<sup>34</sup> and we refer interested readers to that work for the details of that potential. The CaF<sup>+</sup> multipole moments are calculated directly from this potential by integrating over a sphere at a fixed radius about the center of mass, according to

$$Q_\ell = \frac{2\ell + 1}{2} \int_0^\pi d\theta \sin \theta \Phi(r, \theta) r^{\ell+1} P_\ell(\cos \theta). \quad (60)$$

These results are shown in the second column of Table II. The multipole moments calculated according to this method are expected to be far more accurate than those generated by the point-charge model, but may be somewhat limited in accuracy compared to those generated using all-electron *ab initio* methods.

In addition to the above one-electron *ab initio* calculations, a set of all-electron *ab initio* calculations were performed. Details and results of these calculations will be reported elsewhere,<sup>35</sup> but we summarize the results here. In this set of calculations, CCSD(T) *ab initio* methods (using an updated cc-pCVTZ basis for the calcium atom<sup>36</sup>) were used to determine a new effective one-electron potential energy surface for the  $e^-/\text{CaF}^+$  system by placing a test charge on various points along a grid about the CaF<sup>+</sup> core and calculating a single-point energy at each grid location. Multipole moments about the equilibrium internuclear distance  $R_e = 3.54 a_0$  are then calculated according to Eq. (60), but in this case a Fourier interpolation method<sup>37</sup> is applied to provide continuous sampling. The results are shown in the third column of Table II. Of the three computational methods used to calculate the multipole moments of the CaF<sup>+</sup> core, this method is expected to be the most accurate.

As Table II illustrates, the point-charge model overestimates the values of all core electric multipole moments, and we can use the values generated by this method to calculate a safe upper limit on the values of the *actual* electric multipole matrix elements. The magnitudes of the electric multipole matrix elements, calculated using the point-charge multipole moments in the first column of Table II, are shown in Table III.

### F. Application of extended long-range model to *f*, *g*, and *h* Rydberg series of CaF

The *nf* and *ng* Rydberg states identified in Sec. III A were fit to an effective Hamiltonian using the matrix elements given in Eqs. (56) and (57). Three fit iterations were required in the case of the *nf* states and two were required in the case of the *ng* states. The effective tensor coefficients  $C^{(i)}$  and orbit-rotation drag coefficients  $\eta$  for the 13*f* and 13*g* complexes are summarized in Table IV.

The first long-range interaction which can be separated using the effective tensor coefficients determined from the fit is the isotropic polarizability. Whereas the scalar contributions of the permanent electric multipole fields to the energies of the *nf* states, assuming point-charge behavior, are on the order of 0.1 cm<sup>-1</sup>, the same contributions to the energy splittings of the *ng* states are approximately one order of magnitude smaller and will be unobservable at the resolution of the experiments described in this work. Thus, for the *ng* states, the entire scalar contribution effectively arises from the isotropic dipole polarizability. Equating the scalar tensor coefficient for the *ng* states with the expression for the isotropic dipole polarization matrix element, Eq. (16), gives an isotropic polarizability of  $\alpha = 14.87 \pm 0.28$  a.u.

TABLE III. Magnitudes of long-range matrix elements of electric multipole fields and dipole polarizabilities for  $\ell=3, 4$ , and 5 in  $\text{cm}^{-1}$ . All magnitudes are given for  $n=13$  and  $\lambda=0$ . Electrostatic matrix elements are calculated using point-charge multipole moments given in Table II, and polarization matrix elements are calculated assuming  $\alpha=15a_0^3$  and  $\gamma=5a_0^3$ .

Order	Term	Rank	Magnitude ( $\ell=3$ )	Magnitude ( $\ell=4$ )	Magnitude ( $\ell=5$ )
1	Quadrupole	2	-2.00	-0.908	-0.4980
	Hexadecapole	4	-0.27	-0.036	-0.0076
2	Dipole	0	0.00	0.000	0.0000
		2	13.90	6.315	3.401
	Quadrupole	0	0.04	0.006	0.0014
		2	0.09	0.015	0.0035
		4	-0.11	0.004	0.0031
	Dipole-Octupole	2	-0.05	-0.004	-0.0005
		4	-0.16	-0.014	-0.0021
	Octupole	0	-0.09	-0.006	-0.0008
		2	0.03	0.001	0.0001
		4	-0.04	0.001	0.0002
		6	0.17	0.004	0.0004
	Isotropic	0	-2.32	-0.623	-0.2190
	Polarizability				
	Anisotropic	2	-0.14	-0.036	-0.0120
	Polarizability				

The next step in the analysis involves separating the electronic energy splittings due to the anisotropic multipole fields from those due to the anisotropic dipole polarizability. In principle this is accomplished using the second-rank tensor coefficients. For both the  $nf$  states and  $ng$  states, the electric dipole moment, electric quadrupole moment, and anisotropic dipole polarization terms give rise to the primary second-rank tensor contributions. Therefore, to the extent that the long-range model is valid, the second-rank tensor coefficients may be equated with the matrix elements of the contributing long-range interactions to determine  $\mu$ ,  $Q$ , and  $\gamma$ ,

$$\frac{C_{\ell}^{(2)}}{n^3} = (\mu^2 - Q) \frac{2}{n^3(2\ell+3)(2\ell+1)(2\ell-1)\ell(\ell+1)} - \gamma \frac{4(\ell(\ell+1) - 3n^2)}{3n^5(2\ell+3)^2(2\ell+1)(2\ell-1)^2\ell(\ell+1)} \quad (61)$$

or, explicitly for  $n=13$ ,  $\ell=3$  and  $n=13$ ,  $\ell=4$ ,

$$C_{\ell=3}^{(2)} = (\mu^2 - Q) + 0.0437\gamma, \quad (62)$$

$$C_{\ell=4}^{(2)} = (\mu^2 - Q) + 0.0250\gamma.$$

Unfortunately, the anisotropic polarizability determined using Eq. (62) and the tensor coefficients determined from the

fitted data is unreasonably large (approximately 50 a.u.) and implies, in combination with the isotropic polarizability determined above, that the polarizability of the  $\text{CaF}^+$  core in a direction perpendicular to the internuclear axis [ $a_{\perp}$ ; see Eqs. (18) and (19)], is negative, which is an unphysical result.

The reason for this discrepancy is quite simply that the  $nf$  states of  $\text{CaF}$  are not perfectly nonpenetrating. Some additional level shifts and splittings exist and are due to core-penetration effects, which are by definition outside the scope of the long-range model. We arrive at this conclusion for several reasons. First of all, an anisotropic polarizability of 50 a.u. for  $\text{CaF}^+$  is quite unexpected; calculations<sup>38,39</sup> of the anisotropic polarizabilities of the alkali fluorides and chlorides predict anisotropic polarizabilities of 0–10 a.u. for first-, second-, and third-row fluorides and chlorides (smaller for lighter fluorides and larger for heavier chlorides). The behavior displayed by the alkali halides should be quite similar to that of  $\text{CaF}^+$ , and especially so for  $\text{KF}$ , which is isoelectronic with  $\text{CaF}^+$ . According to the calculations, the anisotropic polarizability of  $\text{KF}$  is approximately 1.5 a.u. (Ref. 38) and its dipole moment is approximately 3.35 a.u. For comparison, the dipole moment of  $\text{CaF}^+$  is calculated to be almost exactly 3.35 a.u. using the methods outlined in Sec. III E (see Table II). It is therefore reasonable to expect that the anisotropic polarizability should be approximately 1.5 a.u., and certainly cannot be larger than 5 a.u. An anisotropic polarizability of 5.0 a.u. would give level splittings on the order of 0.1  $\text{cm}^{-1}$  for 13 $f$ , which would be small but detectable at our resolution and precision. By contrast, the discrepancies here between the observed and predicted behavior, as we will see below, are on the order of 1.0  $\text{cm}^{-1}$ . The observed deviations therefore cannot be due to the anisotropic polarizability, and as discussed in Sec. III C, higher-order polarization terms should be entirely negligible.

TABLE IV. Fit parameters for 13 $f$  and 13 $g$  Rydberg states of  $\text{CaF}$ . The tensor coefficients  $C^{(n)}$  are given in  $\text{cm}^{-1}$  and  $\eta$  is dimensionless.

Parameter	13 $f$	13 $g$
$C^{(0)}$	$-3708.63 \pm 25.59$	$-1412.99 \pm 26.79$
$C^{(2)}$	$1182.81 \pm 5.34$	$355.53 \pm 3.58$
$C^{(4)}$	$10.65 \pm 0.23$	...
$\eta$	$0.9752 \pm 0.0009$	$0.9989 \pm 0.0006$



We can also rule out higher-order multipole moments as the cause of the deviations. As discussed in Sec. III E, the multipole moments calculated according to the point-charge model should be regarded as upper bounds, and therefore matrix elements of the octupole and hexadecapole operators can be no larger than  $0.25 \text{ cm}^{-1}$  for  $13f$ , which is still at least four times smaller than the observed deviations.

Finally, the notion that  $nf$  states of CaF can be slightly core penetrating may be argued by estimating the fraction of the electron wavefunction that lies inside the core using simple hydrogenic wavefunctions. Approximating the core boundary as a spherical surface with a radius of  $5a_0$  (approximately the distance between the  $\text{Ca}^{2+}$  nucleus and the outer edge of the  $\text{F}^-$  ion), the fraction of a hydrogenic  $13s$  orbital lying inside the core is approximately  $9.7 \times 10^{-4}$ , or approximately 0.1%. Similarly, the fractions for  $13p$ ,  $13d$ ,  $13f$ , and  $13g$  are  $9.9 \times 10^{-4}$ ,  $9.1 \times 10^{-4}$ ,  $8.5 \times 10^{-5}$ , and  $1.9 \times 10^{-6}$ , respectively, and the corresponding percentages are approximately 0.1%, 0.1%, 0.01%, and 0.0001%. The penetration fractions for  $13s$ ,  $13p$ , and  $13d$  are therefore approximately equal, whereas the fraction for  $13f$  is an order of magnitude smaller, and the fraction for  $13g$  is *three* orders of magnitude smaller. On these grounds we therefore expect the  $nf$  states to be very weakly penetrating, and the  $ng$  states to exhibit almost completely nonpenetrating behavior.

Since the  $nf$  states of CaF exhibit some symptoms of core penetration, it is not possible to apply the long-range model described in Secs. III B and III C. On the other hand, the  $nh$  states, at our experimental precision, cannot provide accurate estimates of *any* of the electric multipole moments or polarizabilities, simply because their matrix elements for  $\ell=5$  are too small. We are therefore unable to rigorously determine a value for the anisotropic dipole polarizability.

However, the  $ng$  states are still amenable to a fit using the long-range model, and we may still use them to determine an accurate value of  $(\mu^2 - Q)$ . [Note that  $(Q - \mu^2)$  is equal to the quadrupole moment calculated in a coordinate system with the origin located at the *center of charge*]. As noted above, it is reasonable to assume that  $\gamma \approx 1.5 \text{ a.u.}$ , which gives electronic splittings on the order of  $0.02 \text{ cm}^{-1}$ , significantly below our sensitivity limit. Therefore we make the approximation

$$C_{\ell=4}^{(2)} = (\mu^2 - Q) + 0.0250\gamma \approx (\mu^2 - Q), \quad (63)$$

which gives  $(\mu^2 - Q) = 11.23 \pm 0.11 \text{ a.u.}$

While it is not possible, on the basis of the data described here, to determine values for the higher-order multipole moments, such a determination should be possible using higher-resolution sources and/or in ultrahigh resolution experiments such as those described by Merkt and co-workers.<sup>40–43</sup>

The observed energy levels of several of the  $nf$ ,  $ng$ , and  $nh$  complexes are plotted against the predictions of the long-range model using the fitted values of  $(\mu^2 - Q)$  and  $\alpha$  in Figs. 2–4. As is evident in the figures, the agreement for the  $ng$  and  $nh$  states is striking, whereas nearly all of the  $nf$  states (at low  $N$ ) deviate significantly from long-range behavior.

## G. Analysis of core-penetration effects: States of high orbital angular momentum

Having identified the differences between the observed splittings of the  $nf$  states and those predicted by the long-range model as due to core-penetration effects, we turn now to analyze those effects in detail.

For CaF, there are two possible zero-order pictures in which core-penetration effects can be understood: The hydrogenic framework and the ligand field theory framework. In the hydrogenic framework, hydrogenic orbitals are taken as a starting point and all long-range and penetration effects are understood in terms of deviation from hydrogenic behavior. In the ligand field framework,<sup>44–46</sup> which is only valid for ionic molecules, metal ion orbitals (in this case  $\text{Ca}^+$ ) are assumed to be mixed by the electric field of an attached ligand (in this case of  $\text{F}^-$ ), which is often treated as a point charge.

Penetration effects in the hydrogenic picture for the NO molecule have been discussed extensively by Jungen.<sup>11</sup> In the hydrogenic picture, deviations from the long-range model arise from five sources: (i) Increased effective nuclear charge  $Z_{\text{eff}}(r < r_c) > 1$  experienced by the Rydberg electron inside the core, (ii) exchange interactions between the Rydberg and core electrons, (iii) nonorthogonality of the Rydberg and core electron orbitals (Pauli repulsion), (iv)  $\ell$  mixing of the Rydberg orbitals at short range by the electric field of the core, and (v) electron correlation. The first effect, increased effective nuclear charge, is due to the incomplete screening of the nucleus by the core electrons when the electron enters the core region. It is always a stabilizing effect (i.e., contributes positively to the quantum defect). The second and third effects arise due to the nonzero overlap between the Rydberg electron and core electron orbitals. The exchange interaction is likewise always stabilizing. The nonorthogonality effect represents an attempt by the molecule to satisfy the Pauli exclusion principle, and gives rise to “Pauli repulsion.” Pauli repulsion is always a destabilizing effect. The fourth effect,  $\ell$  mixing of the Rydberg orbitals at short range, is simply the result of the Rydberg electron entering the nonspherical Hartree-Fock field of the ion core. It is distinct from  $\ell$  mixing at long range in the sense that when  $r$  is on the order of  $R$ , the multipole expansion of Eq. (4) is not valid and cannot be used to calculate the matrix elements of the electrostatic interactions at short range. Finally, the fifth effect, electron correlation, involves the concerted motion of two electrons which, in Rydberg molecules, implies electronic excitation of the core.

In CaF, the core (in its ground electronic state) consists of two closed-shell ions,  $\text{Ca}^{2+}$  and  $\text{F}^-$ . Penetration into the fluoride ion is minimized by the overall negative charge of the  $\text{F}^-$  ion and is therefore unlikely to occur. The Rydberg electron should therefore not experience an increased effective nuclear charge due to the presence of the fluorine nucleus. However, exchange always occurs to some extent, and nonorthogonality of the Rydberg orbital with the occupied  $\text{F}^- 2p$  orbitals must be considered for  $\sigma$  and  $\pi$  Rydberg orbitals, regardless of  $\ell$ . The presence of the  $\text{F}^-$  ion also gives rise to a strong inhomogeneous electric field which will

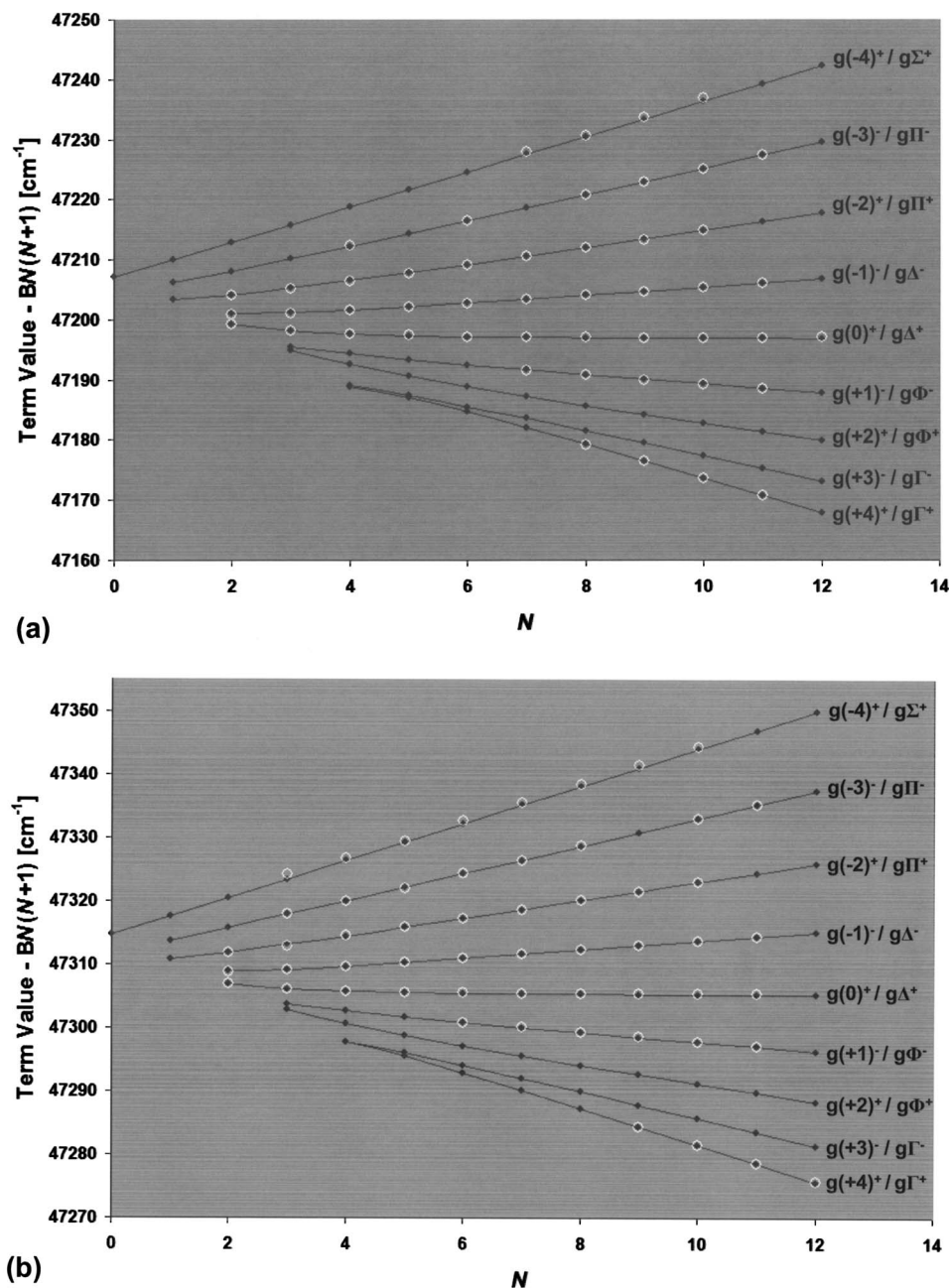


FIG. 2. (a) Observed energy levels of the 15g complex. (b) Observed energy levels of the 17g complex. Open circles indicate observed energy levels and closed connected circles indicate calculated energy levels. Hund's case (d) labels  $\ell(\ell_R)^\pm$  and case (b) labels  $\ell\lambda^\pm$  are for each component of each complex.

significantly mix Rydberg orbitals of any symmetry. Penetration into the positively charged  $\text{Ca}^{2+}$  ion is significant, especially for states with  $\ell < 3$ , and therefore increased effective nuclear charge and exchange must be taken into account in the hydrogenic picture. Since the  $s$  and  $p$  core orbitals of the  $\text{Ca}^{2+}$  ion are occupied, the possible nonorthogonality of  $s$  and  $p$  Rydberg orbitals with  $s$  and  $p$  core orbitals must also be considered. Finally, effect ( $v$ ), electron correlation, is a potential source of deviations from hydrogenic behavior in the sense that the Rydberg electron can excite the core and transfer charge from the  $\text{F}^-$  to  $\text{Ca}^{2+}$ , leading to amplitude in the  $\text{Ca}^+\text{F}^0$  configuration, which is unstable and will typically lead to dissociation of the molecule into neutral Ca and F fragments.

In the ligand field picture, on the other hand, many of these effects are already accounted for in zero order. Since the starting point of the ligand field picture is the set of

eigenstates of the potassium-like  $\text{Ca}^+$  ion, all effects associated with penetration into the  $\text{Ca}^{2+}$  closed shell core are already accounted for. Therefore, we need only concern ourselves with the effects due to the presence of the  $\text{F}^-$  ion. We will therefore adopt the ligand field picture as our zero-order framework, since this will considerably simplify our discussion of penetration effects.

The observed energy levels of the 13f and 15f complexes and their positions calculated using the parameters determined in Sec. III F are shown in Figs. 4(a) and 4(b). As the figures show, the centers of gravity of the  $f$  complexes (located approximately at the high- $N$  asymptote of the  $\Delta^-$  component), match the calculations almost perfectly. The measured isotropic polarizability gives, for the  $f$  states of CaF, an isotropic contribution to the quantum defect of 0.023, which is in excellent agreement with the quantum defect of 0.025 for the  $f$  series of  $\text{Ca}^+$ . In  $\text{Ca}^+$  the quantum

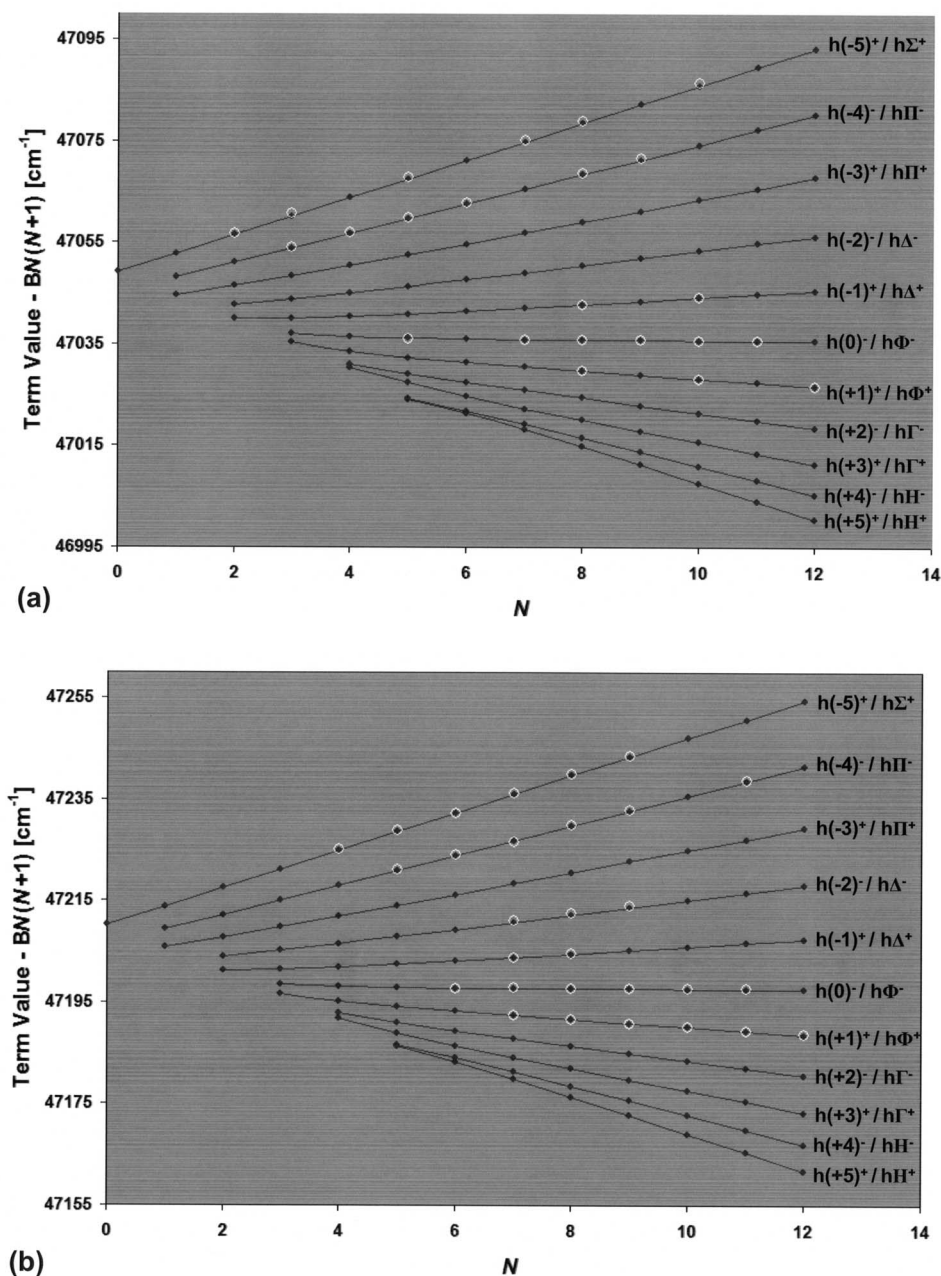


FIG. 3. (a) Observed energy levels of the 13h complex. (b) Observed energy levels of the 15h complex. Open circles indicate observed energy levels and closed connected circles indicate calculated energy levels. Hund's case (d) labels  $\ell(\ell_R)^\pm$  and case (b) labels  $\ell\lambda^\pm$  are for each component of the complex.

defect of the  $f$  series is known to be caused almost entirely by polarization, and we can therefore conclude that the polarization interaction between the Rydberg electron and the  $\text{Ca}^{2+}$  core is responsible for the isotropic shift observed here. The  $\text{F}^-$  ion contributes very little in this respect.

While the isotropic shift of the complex is accounted for in zero order, almost all components of the 13f and 15f complexes deviate significantly from their expected positions. The  $\Sigma^+$ ,  $\Pi^+$ ,  $\Pi^-$ ,  $\Phi^+$ , and  $\Phi^-$  components all lie higher in energy than the long-range model predicts, and the  $\Delta^+$  and  $\Delta^-$  components lie slightly lower in energy than the long-range model predicts. The 14f, 16f, and 17f complexes, shown in the supplementary material, obey the same trends. Thus, while the scalar contribution to the  $\ell=3$  quantum defects is almost entirely due to long-range interactions with the  $\text{Ca}^{2+}$  core, the tensor contributions are due partly to the

long-range fields and partly to short-range interaction with the  $\text{F}^-$  ion. As noted above, the additional short-range interactions with  $\text{F}^-$  can arise from exchange, nonorthogonality,  $\ell$  mixing, and electron correlation. Since the  $2p$  shell of the  $\text{F}^-$  ion is closed, exchange should be negligible. Pauli repulsion, which is a destabilizing interaction, is only a source of concern for the  $\Sigma$  and  $\Pi$  components. As both of these components of the  $f$  complexes lie significantly higher in energy than predicted by the long-range model, it is likely that at least part of the discrepancy is accounted for by Pauli repulsion due to nonorthogonality of the Rydberg and  $\text{F}^-$  orbitals.

The bulk of the deviations from long-range behavior, however, are most likely due to  $\ell$  mixing at short range. The  $\Delta$  and  $\Phi$  components of the  $f$  complex, by symmetry, cannot suffer the effects of electron correlation or nonorthogonality, and the only source of deviation is therefore  $\ell$  mixing, which



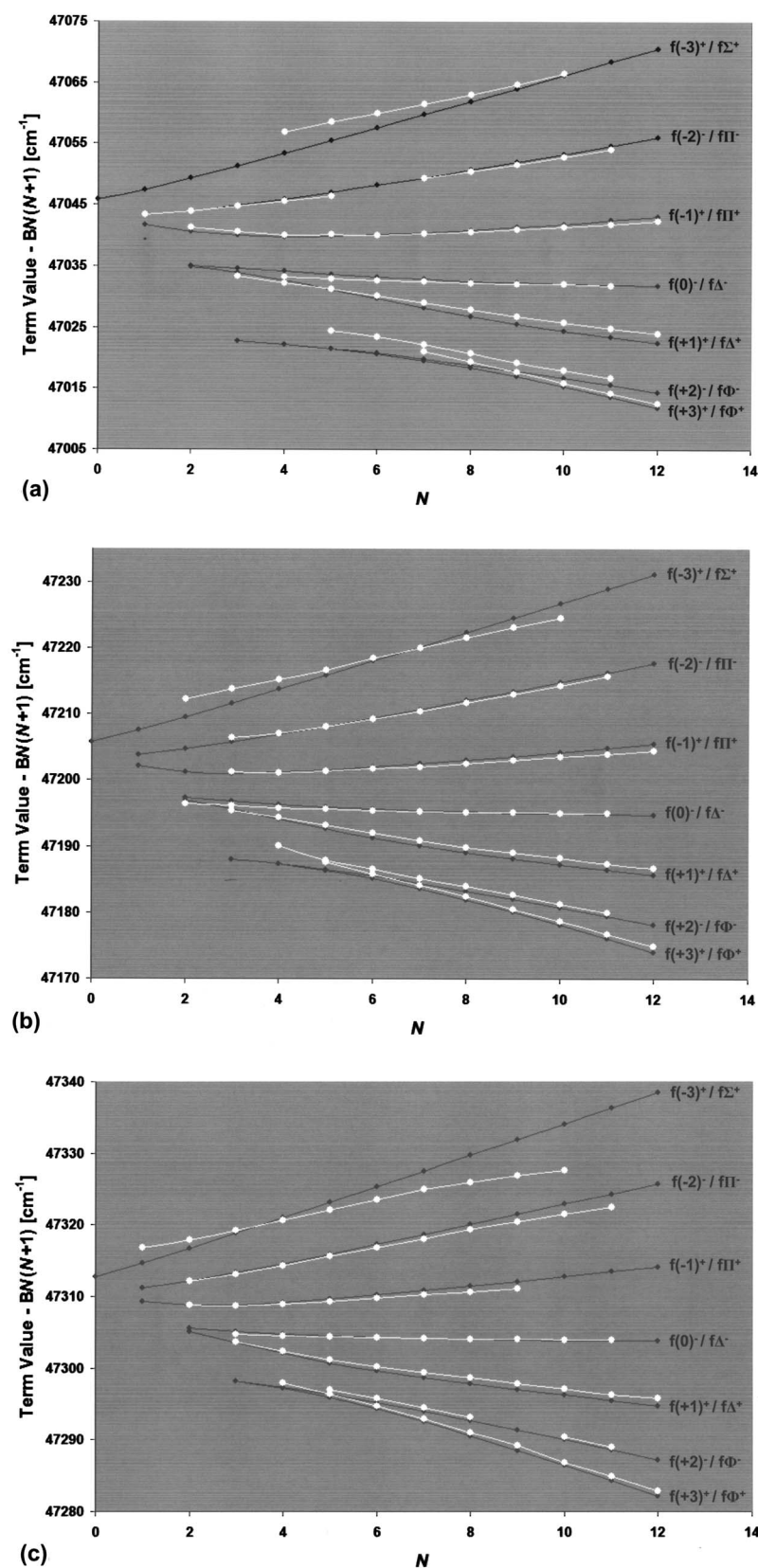


FIG. 4. (a) Observed energy levels of the  $13f$  complex. (b) Observed energy levels of the  $15f$  complex. (c) Observed energy levels of the  $17f$  complex. Connected white circles indicate observed energy levels and connected black circles indicate calculated energy levels. Hund's case (d) labels  $\ell(\ell_R)^\pm$  and case (b) labels  $\ell\lambda^\pm$  are for each component of the complex.

can be a stabilizing or destabilizing interaction. Since this  $\ell$  mixing causes deviations from long-range behavior for  $f\Delta$  and  $f\Phi$  that are similar in magnitude to the deviations for  $f\Sigma$  and  $f\Pi$ , it appears likely that the bulk of *all* of the penetration effects in the  $f$  complexes are accounted for by  $\ell$  mixing at short range.

#### H. Analysis of core-penetration effects: States of low orbital angular momentum

While no spectroscopic investigations of states with  $\ell < 3$  are presented in this paper, the discussion in Sec. III G allows us to begin to understand what fractions of the (much



TABLE V. Contributions to the quantum defects of the  $nd$  series of CaF.

Series	Quantum defect	$\delta$ , Ca <sup>+</sup>	$\delta$ , long range	$\delta$ , short range
$d\Sigma$	-0.19	0.62	-0.22	-0.59
$d\Pi$	1.02	0.62	-0.11	0.51
$d\Delta$	0.86	0.62	0.21	0.03

larger) quantum defects of the core-penetrating “ $s$ ,” “ $p$ ,” and “ $d$ ” series of CaF are due to long-range interactions and what fractions are due to penetration effects.

Of all of the series of CaF with  $\ell < 3$ , the  $nd$  states should exhibit the weakest penetration effects and should therefore be most amenable to the perturbation treatment employed in this investigation. Of the three, the  $d\Delta$  series of CaF should be the most weakly penetrating, and by symmetry can only be affected by  $\ell$  mixing at short range. The quantum defects of the  $d\Sigma$ ,  $d\Pi$ , and  $d\Delta$  series of CaF and their origins are summarized in Table V. The quantum defect of the  $d$  series of Ca<sup>+</sup> is 0.62, and the quantum defects of the  $d\Sigma$ ,  $d\Pi$ , and  $d\Delta$  series of CaF are -0.19, 1.02, and 0.86, respectively. The long-range contributions to the quantum defects (including only the contributions due to the electric dipole and quadrupole fields) are -0.22, -0.11, and 0.21, which means that the short-range contributions for  $\Sigma$ ,  $\Pi$ , and  $\Delta$  are -0.59, 0.51, and 0.03. Thus, the  $d\Delta$  series of CaF is indeed a long-range series and exhibits only very weak core penetration. On the other hand the  $\Sigma$  and  $\Pi$  series, as expected, are much more strongly core penetrating.

As shown in Appendix B, while the agreement of the perturbation method is excellent for  $f$  and  $g$  states, the agreement is reasonable for  $d$  states and is rather poor for  $s$  and  $p$  states. However, the contributions to the quantum defects from the dipole field can be determined exactly, and for the sake of the following discussion we will assume that the dipole field is the only long-range interaction that contributes significantly to the quantum defects. The quantum defects of the  $s\Sigma$ ,  $p\Sigma$ , and  $p\Pi$  series of CaF and their origins are summarized in Table VI. As can be seen in the table, for the  $p$  states the long-range contributions from the dipole field are nearly as large as the short-range contributions, and in this case they are of opposite sign. For  $s$  states, it is not possible

TABLE VI. Contributions to the quantum defects of the  $ns$  and  $np$  series of CaF.

Series	Quantum defect	$\delta$ , Ca <sup>+</sup>	$\delta$ , long range	$\delta$ , short range
$s\Sigma$	2.45	1.80	...	...
$p\Sigma$	2.12	1.45	-1.09	1.76
$p\Pi$	1.64	1.45	1.42	-1.23

to analytically calculate the contribution from the dipole field when the dipole moment is greater than 0.64 a.u.,<sup>5</sup> and thus for the  $s$  states we are not able to separate the long-range and short-range contributions.

#### IV. CONCLUSION

We have analyzed the  $f$ ,  $g$ , and  $h$  Rydberg states of CaF and separated the contributions of the various long-range and short-range interactions to their quantum defects. Our extensions to the long-range model have not only made it possible for us to positively identify evidence of core penetration of the  $f$  orbitals, but should also be useful in the analysis of ultrahigh resolution spectra of nonpenetrating states with very high orbital angular momentum. The analysis presented in this paper will ultimately facilitate a mechanistic understanding of the origins of all of the quantum defects of CaF, as well as their dependence on the internuclear distance  $R$  and the collision energy  $\varepsilon$  of the Rydberg electron.

#### ACKNOWLEDGMENTS

The authors wish to thank Christian Jungen, Stephen R. Lundeen, and James K. G. Watson, for helpful discussions. This work was supported by the National Science Foundation Grant No. CHE-04050876.

#### APPENDIX A: SECOND-ORDER DIPOLE-OCTUPOLE AND SECOND-ORDER OCTUPOLE MATRIX ELEMENTS

The tensor matrix elements of the second-order dipole-octupole cross-term are as follows:

$$\langle \psi_{n\ell\lambda} | V_{13} | \psi_{n\ell\lambda} \rangle^{(2,k=2)} = -\mu \cdot O \frac{4(560\ell^8 + 2240\ell^7 + 4760\ell^6 + 6440\ell^5 + 1799\ell^4 - 4522\ell^3 - 2700\ell^2 + 261\ell + 162)}{n^3 \sqrt{21}(2\ell+3)^4(2\ell+1)^3(2\ell-1)^4\ell^3(\ell+1)^3(\ell+2)(\ell-1)} \times \{\ell(\ell+1) - 3\lambda^2\}, \quad (\text{A1})$$

$$\langle \psi_{n\ell\lambda} | V_{13} | \psi_{n\ell\lambda} \rangle^{(2,k=4)} = -\mu \cdot O \times \frac{2\sqrt{\frac{3}{7}}(2240\ell^{10} + 11200\ell^9 + 11760\ell^8 - 20160\ell^7 - 48636\ell^6 - 28308\ell^5 + 10921\ell^4 + 23102\ell^3 + 8235\ell^2 - 1314\ell - 540)}{n^3(2\ell+5)(2\ell+3)^4(2\ell+1)^3(2\ell-1)^4(2\ell-3)\ell^3(\ell+1)^3(\ell-1)^2(\ell+2)^2} \times \{35\lambda^4 - 5(6\ell(\ell+1) - 5)\lambda^2 + 3(\ell+2)(\ell-1)\ell(\ell+1)\}. \quad (\text{A2})$$

The scalar and tensor matrix elements of the electric octupole interaction in second-order are as follows: The scalar part is

$$\begin{aligned}
\langle \psi_{n\ell\lambda} | V_{33}(r) | \psi_{n\ell\lambda} \rangle^{(2,k=0)} &= -O^2 \frac{2}{n^3} (4480\ell^{12} + 29568\ell^{11} + 33824\ell^{10} - 128352\ell^9 - 311304\ell^8 - 56952\ell^7 + 410102\ell^6 + 425670\ell^5 + 27805\ell^4 \\
&\quad - 217824\ell^3 - 101727\ell^2 + 11070\ell + 5940) \times ((2\ell+5)^2(2\ell+3)^3(2\ell+1)^4(2\ell-1)^3(2\ell-1)^2\ell^2(\ell+1)^2(\ell+2)^2(\ell-1)^2)^{-1}.
\end{aligned} \quad (\text{A3})$$

The second-rank tensor part is

$$\begin{aligned}
\langle \psi_{n\ell\lambda} | V_{33}(r) | \psi_{n\ell\lambda} \rangle^{(2,k=2)} &= O^2 \frac{6}{n^3} (8960\ell^{12} + 53760\ell^{11} + 76160\ell^{10} - 112000\ell^9 - 494144\ell^8 - 713216\ell^7 + 77912\ell^6 + 1668232\ell^5 \\
&\quad + 1159673\ell^4 - 773446\ell^3 - 663261\ell^2 + 41970\ell + 36900) ((2\ell+5)^2(2\ell+3)^4(2\ell+1)^3(2\ell-1)^4 \\
&\quad \times (2\ell-3)^2\ell^3(\ell+1)^3(\ell+2)^2(\ell-1)^2)^{-1} \{\ell(\ell+1) - 3\lambda^2\}.
\end{aligned} \quad (\text{A4})$$

The fourth-rank tensor part is

$$\begin{aligned}
\langle \psi_{n\ell\lambda} | V_{33}(r) | \psi_{n\ell\lambda} \rangle^{(2,k=4)} &= O^2 \frac{6}{11n^3} (216832\ell^{14} + 1517824\ell^{13} - 394240\ell^{12} - 22097152\ell^{11} - 41698272\ell^{10} + 30240672\ell^9 \\
&\quad + 166914704\ell^8 + 181132160\ell^7 - 63820889\ell^6 - 390231083\ell^5 - 235477683\ell^4 + 175848759\ell^3 \\
&\quad + 141160248\ell^2 - 9510480\ell - 7889400) ((2\ell+5)^3(2\ell+3)^4(2\ell+1)^3(2\ell-1)^4(2\ell-3)^3\ell^3(\ell+1)^3 \\
&\quad \times (\ell+2)^3(\ell-1)^3)^{-1} \{35\lambda^4 - 5(6\ell(\ell+1) - 5)\lambda^2 + 3(\ell+2)(\ell-1)\ell(\ell+1)\}.
\end{aligned} \quad (\text{A5})$$

The sixth-rank tensor part is

$$\begin{aligned}
\langle \psi_{n\ell\lambda} | V_{33}(r) | \psi_{n\ell\lambda} \rangle^{(2,k=6)} &= O^2 \frac{15}{n^3\ell^3} (118272\ell^{16} + 946176\ell^{15} + 453376\ell^{14} - 13348448\ell^{13} - 22959552\ell^{12} + 79291520\ell^{11} \\
&\quad + 221067968\ell^{10} - 53247744\ell^9 - 624008242\ell^8 - 554534728\ell^7 + 329251941\ell^6 + 1043332267\ell^5 \\
&\quad + 495866797\ell^4 - 452547543\ell^3 - 325608060\ell^2 + 24327000\ell + 18333000) \\
&\quad \times [(2\ell+7)(2\ell-5)(\ell+3)(\ell-2)]^{-1/2} [(2\ell+3)(2\ell-1)]^{-(7/2)} [(2\ell+5)(2\ell+1)(2\ell-3)(\ell+2)(\ell+1) \\
&\quad \times (\ell-1)]^{-(5/2)} (128\ell^{12} + 832\ell^{11} - 416\ell^{10} - 11440\ell^9 - 10296\ell^8 + 53196\ell^7 + 70642\ell^6 - 99385\ell^5 \\
&\quad - 150007\ell^4 + 68497\ell^3 + 108849\ell^2 - 11700\ell - 18900)^{-(1/2)} \{5\ell^2(63\lambda^4 + 84\lambda^2 + 4) + 15\ell(21\lambda^4 \\
&\quad + 35\lambda^2 + 4) - 21\lambda^2(11\lambda^4 + 35\lambda^2 + 14) - 5\ell^4(21\lambda^2 + 5) - 15\ell^3(14\lambda^2 + 5) + 5\ell^6 + 15\ell^5\}.
\end{aligned} \quad (\text{A6})$$

## APPENDIX B: VALIDITY OF PERTURBATION METHOD WITH STRONG CORE DIPOLE FIELD

Watson<sup>5</sup> shows that the Hamiltonian

$$\hat{H} = -\frac{1}{2}\nabla^2 - \frac{Z}{r} + \frac{\ell^2}{2r^2} - \frac{\mu \cos \theta}{r^2} \quad (\text{B1})$$

is exactly soluble in polar coordinates, and that the resulting quantum defects are approximately

$$\delta_{\ell\lambda} = \ell + \frac{1}{2} - \sqrt{\ell(\ell+1) + \frac{2\mu^2[\ell(\ell+1) - 3\lambda^2]}{\ell(\ell+1)(2\ell-1)(2\ell+3)}} + \frac{1}{4}. \quad (\text{B2})$$

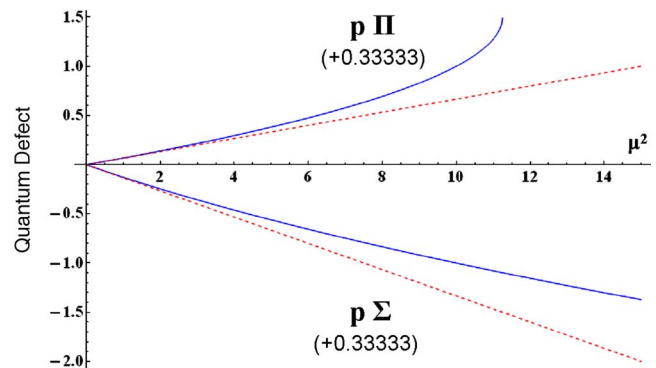


FIG. 5. (Color online) Contribution of the dipole field to the quantum defects for  $\ell=1$ , calculated as a function of  $\mu^2$ : Exact solution (solid lines) and perturbative solution (dashed lines). Numbers in parentheses indicate the difference between the perturbative and exact solutions at  $\mu^2=10$ .

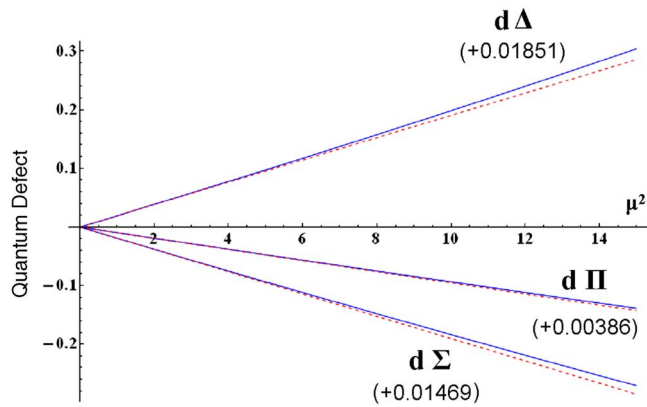


FIG. 6. (Color online) Contribution of the dipole field to the quantum defects for  $\ell=2$ , calculated as a function of  $\mu^2$ : Exact solution (solid lines) and perturbative solution (dashed lines). Numbers in parentheses indicate the difference between the perturbative and exact solutions at  $\mu^2=15$ .

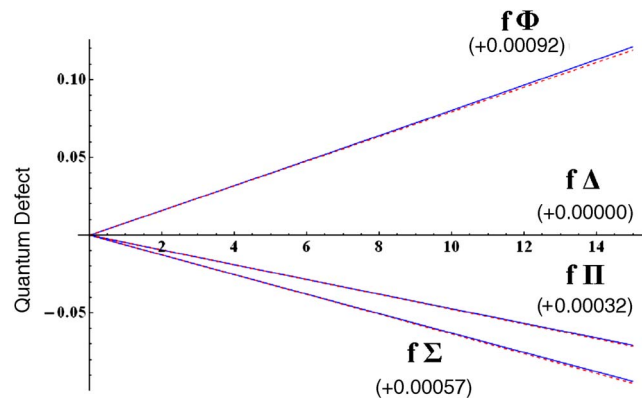


FIG. 7. (Color online) Contribution of the dipole field to the quantum defects for  $\ell=3$ , calculated as a function of  $\mu^2$ : Exact solution (solid lines) and perturbative solution (dashed lines). Numbers in parentheses indicate the difference between the perturbative and exact solutions at  $\mu^2=15$ .

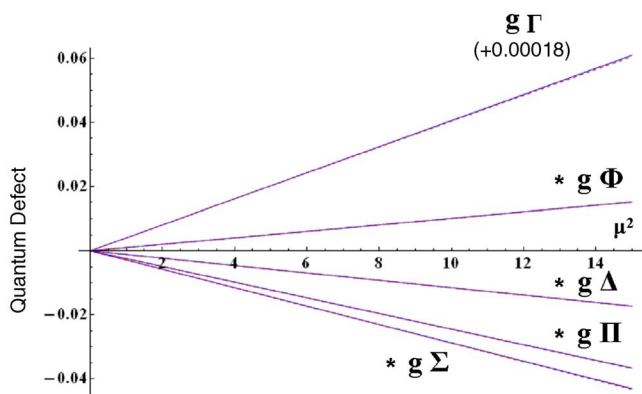


FIG. 8. (Color online) Contribution of the dipole field to the quantum defects for  $\ell=4$ , calculated as a function of  $\mu^2$ : Exact solution (solid lines) and perturbative solution (dashed lines). Numbers in parentheses indicate the difference between the perturbative and exact solutions at  $\mu^2=15$ .

By contrast, the perturbative dipole treatment [Eq. (8)] gives

$$\delta'_{\ell\lambda} = - \frac{2\mu^2[\ell(\ell+1) - 3\lambda^2]}{\ell(\ell+1)(2\ell-1)(2\ell+1)(2\ell+3)}. \quad (\text{B3})$$

The quantum defects predicted by Eqs. (B2) and (B3) are compared in Figs. 5–8 for  $\ell=1, 2, 3$ , and 4, respectively.

<sup>1</sup>Ch. Jungen and E. Miescher, *Can. J. Phys.* **47**, 1769 (1969).

<sup>2</sup>E. E. Eyler and F. M. Pipkin, *Phys. Rev. A* **27**, 2462 (1983).

<sup>3</sup>E. E. Eyler, *Phys. Rev. A* **34**, 2881 (1986).

<sup>4</sup>M. D. Lindsay, A. W. Kam, J. R. Lawall, Ping Zhao, F. M. Pipkin, and E. E. Eyler, *Phys. Rev. A* **41**, 4974 (1990).

<sup>5</sup>J. K. G. Watson, *Mol. Phys.* **81**, 277 (1994).

<sup>6</sup>*Molecular Applications of Quantum Defect Theory*, edited by Ch. Jungen (Institute of Physics, Bristol, 1996).

<sup>7</sup>S. N. Altunata, S. L. Coy, and R. W. Field, *J. Chem. Phys.* **123**, 084319 (2005).

<sup>8</sup>J. J. Kay, D. S. Byun, J. O. Clevenger, X. Jiang, V. S. Petrovic, R. Seiler, J. R. Barchi, A. J. Merer, and R. W. Field, *Can. J. Chem.* **82**, 1 (2004).

<sup>9</sup>V. S. Petrovic and R. W. Field, *J. Chem. Phys.* **128**, 014301 (2008).

<sup>10</sup>H. Lefebvre-Brion and R. W. Field, *Spectra and Dynamics of Diatomic Molecules* (Elsevier, San Diego, 2004).

<sup>11</sup>Ch. Jungen, *J. Chem. Phys.* **53**, 4168 (1970).

<sup>12</sup>G. Herzberg, *Molecular Spectra and Molecular Structure. I. Spectra of Diatomic Molecules* (Krieger, Malabar, FL, 1989).

<sup>13</sup>See EPAPS Document No. E-JCPSA6-128-026817 for additional figures and a complete list of energy levels. For more information on EPAPS, see <http://www.aip.org/pubservs/epaps.html>.

<sup>14</sup>J. D. Jackson, *Classical Electrodynamics* (Wiley, New York, 1975).

<sup>15</sup>J. K. G. Watson, in *The Role of Rydberg States in Spectroscopy and Photochemistry*, edited by C. Sandorfy (Kluwer, Netherlands, 1999), pp. 293–327.

<sup>16</sup>A. R. Edmonds, *Angular Momentum in Quantum Mechanics* (Princeton University Press, Princeton, NJ, 1996).

<sup>17</sup>H. A. Buckmaster, R. Chatterjee, and Y. H. Shing, *Phys. Status Solidi A* **13**, 9 (1972).

<sup>18</sup>A. K. Kazanskiĭ and V. N. Ostrovskiĭ, *Zh. Eksp. Teor. Fiz.* **97**, 78 (1990).

<sup>19</sup>A. K. Kazanskiĭ and V. N. Ostrovskiĭ, *Sov. Phys. JETP* **70**, 43 (1990).

<sup>20</sup>W. G. Sturuss, P. E. Sobol, and S. R. Lundeen, *Phys. Rev. Lett.* **54**, 792 (1985).

<sup>21</sup>W. G. Sturuss, E. A. Hessels, and S. R. Lundeen, *Phys. Rev. Lett.* **57**, 1863 (1986).

<sup>22</sup>W. G. Sturuss, E. A. Hessels, P. W. Arcuni, and S. R. Lundeen, *Phys. Rev. A* **38**, 135 (1988).

<sup>23</sup>P. W. Arcuni, E. A. Hessels, and S. R. Lundeen, *Phys. Rev. A* **41**, 3648 (1990).

<sup>24</sup>W. G. Sturuss, E. A. Hessels, P. W. Arcuni, and S. R. Lundeen, *Phys. Rev. A* **44**, 3032 (1991).

<sup>25</sup>P. L. Jacobson, D. S. Fisher, C. W. Fehrenbach, W. G. Sturuss, and S. R. Lundeen, *Phys. Rev. A* **56**, R4361 (1997).

<sup>26</sup>P. L. Jacobson, R. A. Komara, W. G. Sturuss, and S. R. Lundeen, *Phys. Rev. A* **62**, 012509 (2000).

<sup>27</sup>R. A. Komara, M. A. Gearba, S. R. Lundeen, and C. W. Fehrenbach, *Phys. Rev. A* **67**, 062502 (2003).

<sup>28</sup>E. L. Snow, M. A. Gearba, R. A. Komara, S. R. Lundeen, and W. G. Sturuss, *Phys. Rev. A* **71**, 022510 (2005).

<sup>29</sup>I. Dabrowski, D. W. Tokaryk, M. Vervloet, and J. K. G. Watson, *J. Chem. Phys.* **104**(21), 8245 (1996).

<sup>30</sup>I. Dabrowski, D. W. Tokaryk, and J. K. G. Watson, *J. Mol. Spectrosc.* **189**, 95 (1998).

<sup>31</sup>I. Dabrowski, D. W. Tokaryk, R. H. Lipson, and J. K. G. Watson, *J. Mol. Spectrosc.* **189**, 110 (1998).

<sup>32</sup>I. Dabrowski and D. A. Sadovskii, *J. Chem. Phys.* **107**, 8874 (1997).

<sup>33</sup>I. Dabrowski, D. W. Tokaryk, M. Vervloet, R. H. Lipson, and J. K. G. Watson, in *Spectroscopy: Perspectives and Frontiers*, edited by A. P. Roy (Narosa, New Delhi, 1997).

<sup>34</sup>M. Arif, Ch. Jungen, and A. L. Roche, *J. Chem. Phys.* **106**, 4102 (1997).

<sup>35</sup>S. L. Coy, B. M. Wong, and R. W. Field (unpublished).

<sup>36</sup>M. A. Iron, M. Oren, and J. M. L. Martin, *Mol. Phys.* **101**, 1345 (2003).

<sup>37</sup>Robert Piche, MATLAB, The Mathworks, Natick, MA.

<sup>38</sup>S. L. Davis, *J. Chem. Phys.* **88**, 1080 (1988).

- <sup>39</sup> H. J. Kolker and M. Karplus, *J. Chem. Phys.* **39**, 2011 (1963).
- <sup>40</sup> A. Osterwalder, A. Wüest, F. Merkt, and Ch. Jungen, *J. Chem. Phys.* **121**, 11810 (2004).
- <sup>41</sup> G. M. Greetham, U. Hollenstein, R. Seiler, W. Ubachs, and F. Merkt, *Phys. Chem. Chem. Phys.* **5**, 2528 (2003).
- <sup>42</sup> F. Merkt and A. Osterwalder, *Int. Rev. Phys. Chem.* **21**, 385 (2002).
- <sup>43</sup> A. Osterwalder, R. Seiler, and F. Merkt, *J. Chem. Phys.* **113**, 7939 (2000).
- <sup>44</sup> S. F. Rice, H. Martin, and R. W. Field, *J. Chem. Phys.* **80**, 5023 (1985).
- <sup>45</sup> D. P. Baldwin and R. W. Field, *J. Am. Chem. Soc.* **112**, 9156 (1990).
- <sup>46</sup> C. J. Ballhausen, *Introduction to Ligand Field Theory* (McGraw-Hill, New York, 1962).